37. PALEOMAGNETIC RESULTS, MIDDLE AMERICA TRENCH OFF MEXICO DEEP SEA DRILLING PROJECT LEG 66[1]

Nobuaki Niitsuma, Institute of Geosciences, Shizuoka University, 422 Shizuoka, Japan

INTRODUCTION

This chapter describes the results of a shipboard and shore-based paleomagnetic study of sediments and basement rocks recovered from the outer rise, lower and upper continental slope, Middle America Trench off Mexico (Fig. 1) during Leg 66 of the International Phase of Ocean Drilling of the Deep Sea Drilling Project. The purpose of examining sedimentary sequences is to obtain reliable paleomagnetic data, to establish the magnetostratigraphy of the drilled sediments, and to determine bedding dips and fault planes. Dating sedimentary sequences by means of magnetostratigraphy provides data about the sedimentation rate and the accretionary process along the trench and in the forearc area. Determining the position of geologic structures according to orientation of sedimentary layers and faults provides fundamental information for a reconstruction of the tectonic evolution of this area. I compare magnetic properties of basement rocks with opaque mineral composition of the rocks and ocean magnetic anomalies.

METHODS

Paleomagnetic Techniques

Remanent magnetization of sediment and rock samples was measured with a Digico balanced fluxgate rock magnetometer, calibrated frequently with a shipboard standard. Sensitivity of the magnetometer is inversely proportional to temperature; the negative gradient was $1\%/1°C$ for a standard sample 10^{-3} to 10^{-4} emu/cc in intensity. For samples 10^{-6} emu/cc, there was a negative correlation between sensitivity and temperature, but the linear relationship was disturbed by a fluctuation in sensitivity of a factor of 2. For the samples of less intensity than 10^{-7} emu/cc, there were fluctuations of sensitivity beyond one order of magnitude or more in a linear relationship. Perhaps this fluctuation is one of the causes of the wide range in noise level (1×10^{-7} to 1×10^{-9} emu/cc). Error in direction of remanent magnetization is less than 4°.

I used a Schonstedt A.C. geophysical specimen demagnetizer (Model GSD-1) for alternating field (AF) demagnetization of the samples. With this single axis system demagnetizer, every sample was demagnetized three times, around three orthogonal axes.

A Bison magnetic susceptibility system (Model 3101) was used to measure initial sample susceptibility. Susceptibility was corrected for sample length.

The samples were thermomagnetically analyzed at the Institute of Geosciences, Shizuoka University, with a modified Hirone-type automatic thermomagnetic balance, which records changes in saturation magnetization (Js) and weight of sample with temperature (T) changes. Samples were chips of rock weighing 100 to 400 mg. A field of 5000 Oe was applied during the heating and cooling cycles, but every 5 min. the magnetic field was reduced to zero for 30 s to weigh the sample. The heating and cooling rate was 500°C/hr., and the sample was heated in a vacuum of 10^{-4} torr.

Sampling Procedure

Paleomagnetic samples were taken from unconsolidated and semiconsolidated sediments in the upper parts of the cores by inserting plastic tubes 2.5 cm across and 2.2 cm long into the split sections. The direction of the split planes were determined by continuous marks on the 9.5-meter plastic liners. In more lithified materials at deeper levels, cylindrical samples of diameter 2.5 cm were taken from the split core sections with a diamond corer ("minicore drill"). An orientation was marked with an arrow in the uphole direction on every sample before it was removed from the split core section. When we encountered the inclined bedding, we measured the inclination of bedding plane carefully against the split plane.

In soft, soupy sediments of the upper 20 meters of holes, it was difficult to find original sedimentary structures. From 20 to 80 meters the cored sediments were disturbed along the core liner with marginal laminations concave downward. Below sub-bottom depths of 50 to 200 meters, sediments are broken into pieces several centimeters long which were twisted during drilling rotation. I collected 531 oriented sediment samples selectively from less disturbed parts of cores, especially in the lower part of cores. I took 15 samples of basement rocks, 8 of which were oriented, with a "minicore drill," except for metamorphic rock in Hole 489A for which I used a diamond saw.

REMANENT MAGNETIZATION OF SEDIMENTS

Stability Test of Sediments by AF Demagnetization

The first step in a paleomagnetic study is to eliminate overprinted remanent magnetization from natural remanent magnetization. There are two possible overprinted components in sediment samples: chemical remanent magnetization of goethite and a soft component of remanent magnetization (Niitsuma, 1977). The chemical overprint is caused by precipitation of goethite in an oxidizing atmosphere after deposition of sediments. In this study we can ignore chemical overprint, because the samples were stored in nonoxidizing seawater.

Sediments acquire the soft component of remanent magnetization, consisting of viscous and isothermal remanent magnetization, after deposition mostly in the present magnetic field, even in the course of drilling and sample treatment. The amount and property of the soft component are attributed to type and grain size of magnetic minerals. Because AF demagnetization is effective for analyzing the soft component in remanent magnetization, it is also a check for reliability of remanent magnetization in the paleomagnetic investigation.

As pilot samples from each site, 20 sediment samples were demagnetized in an alternating field increased stepwise. These samples were classified into seven types according to the reaction of remanent magnetization during demagnetization (Figs. 2, 18, and Table 1). Applied AF was 50, 100, 150, 200, and 250 Oe.

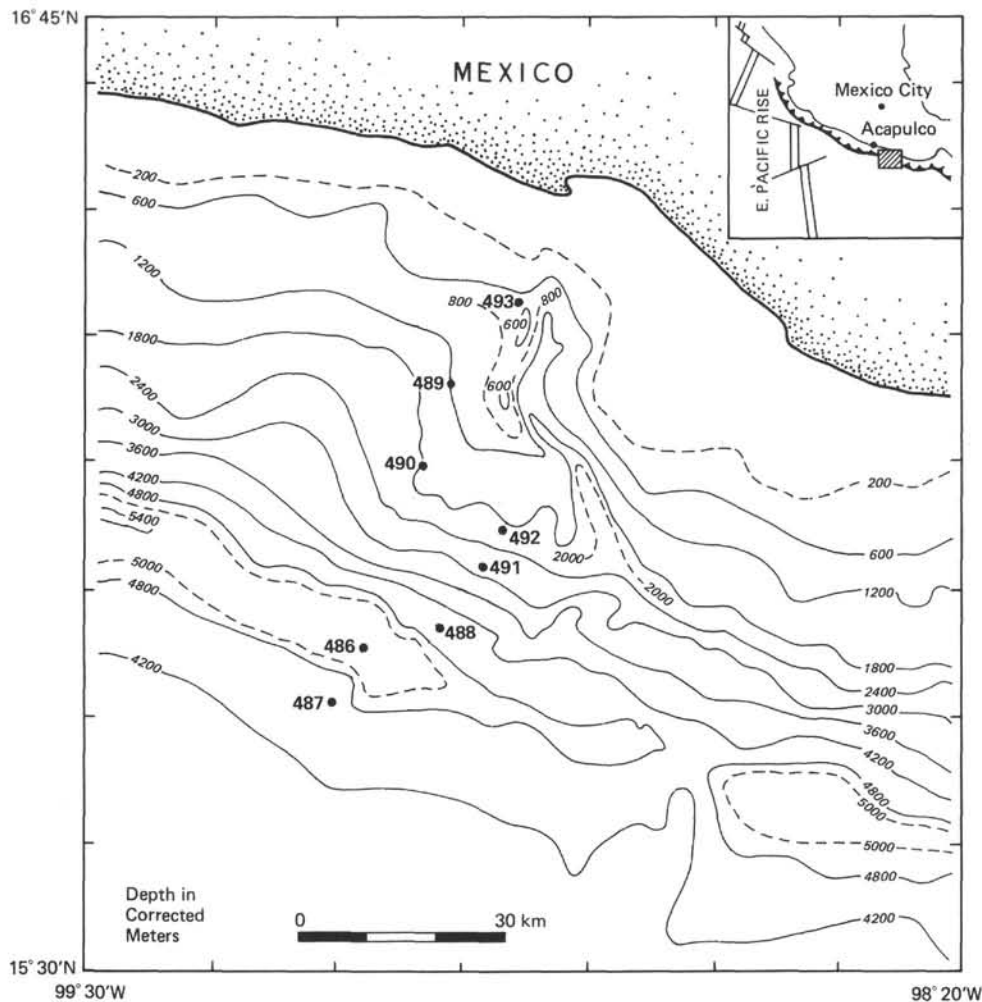*Type A.* This type is characteristic of samples from the outer rise at Site 487. The sediments consist of hemi-

Figure 1. Location of Leg 66 sites.

pelagic mud and brown pelagic clay. Change in direction by AF demagnetization is larger than 20° between 50 and 100 Oe, which is plotted at 75 Oe on the horizontal coordinate in the lower graph of Figure 2, and less than 7° above 100 Oe, the direction becoming stable. Intensity decreases by less than one order by 50 and 100 Oe AF demagnetization but does not change above 100 Oe. Magnetization of Type A samples is reliable for paleomagnetism after 100- or 150-Oe AF demagnetization.

Type T. This type characterizes samples from the lower slope, Sites 488, 491, and 492. Samples of this type consist of muddy silt and muddy siltstone and are from sandy intervals which probably originated in turbidity currents along the Middle America Trench. Change in direction of remanent magnetization was less than 14° through all steps of AF demagnetization. Intensity does not change except in Hole 488 (280.32 m sub-bottom), where sample intensity increases at 150 and 200 Oe. Intensity of samples ranges from 2×10^{-7} to 5×10^{-5} emu/cc. Because the samples of Type T have stable magnetization, they provide reliable paleomagnetism data.

Type P. Samples of this type occurred in the upper part of the lower slope at Site 492. Direction of mag-

netization changes between 10° and 40°. A characteristic minimum value in direction of change occurs at 100- and 150-Oe AF demagnetization. Intensity decrease is within a factor of 3. Pyrite grains and pyrite nodules occur in the sediments including horizons of the present samples. The characteristic high peak in direction change at 200 Oe also occurred in pyrite-rich metamorphic rock from a subdepth of 318.06 meters at Hole 489A. This type of magnetization is probably valid for paleomagnetism after 100- or 150-Oe AF demagnetization.

Type G. This type occurs in sediments from the upper part of the lower slope and the lower part of the upper slope at Sites 490 and 492. Direction change attains a minimum value at 100 Oe and increases suddenly at 150-Oe AF demagnetization. Changes in intensity of remanent magnetization range within a factor of 2. Muddy silty and muddy siltstone of this type contain glauconitic sand grains.

Type S. This type occurs in muddy siltstone and mudstone samples from the upper slope at Sites 490 and 493. Intensity ranges from 1×10^{-7} to 2×10^{-6} emu/cc and decreases monotonously in AF demagnetization steps. The direction of remanent magnetization is relatively stable and changes less than 20° through all steps. At
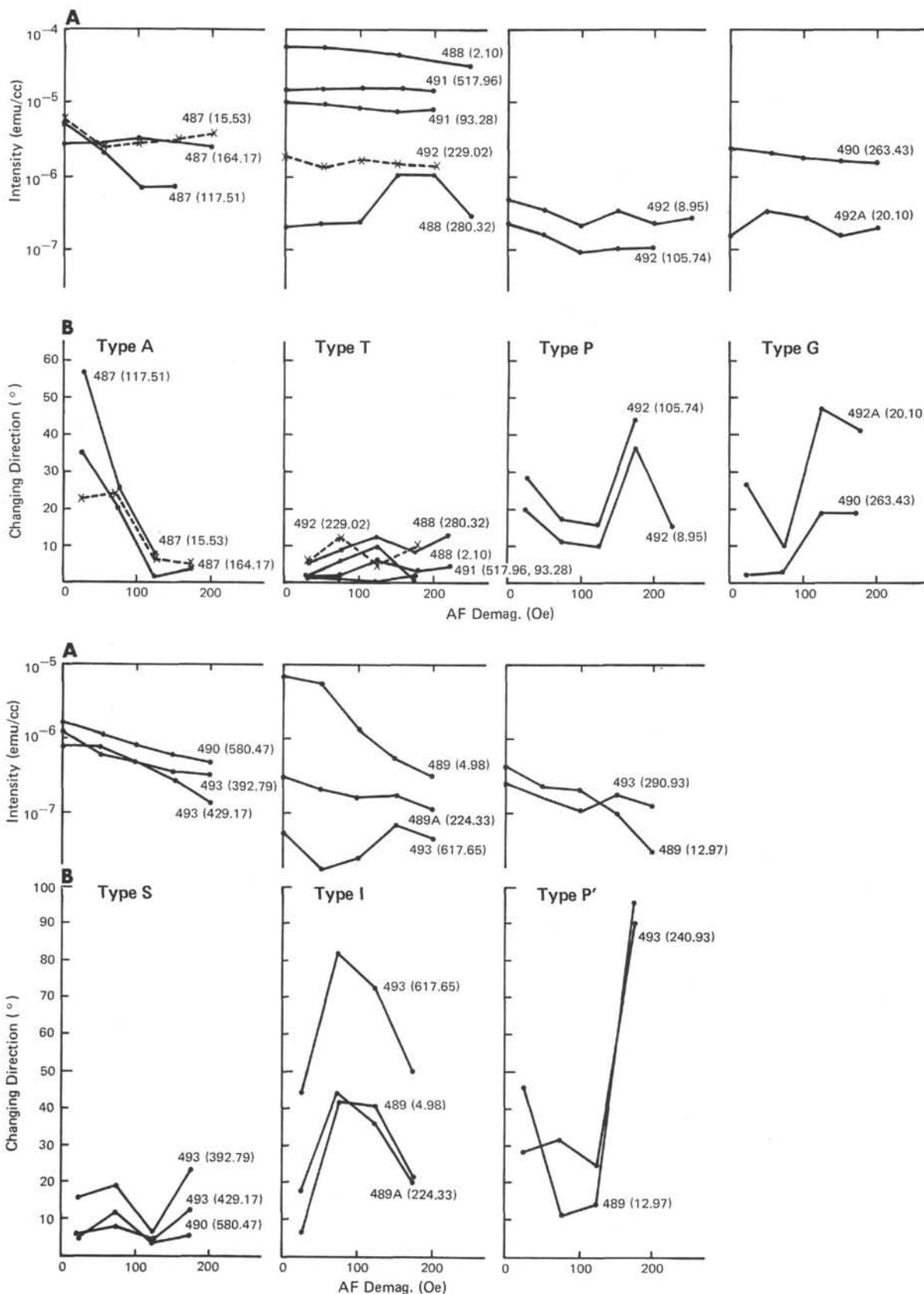
Figure 2. Reaction of remanent magnetization of sediment samples during stepwise AF demagnetization. A. Changes in intensity of remanent magnetization in logarithmic scale. B. Changes in direction of remanent magnetization with each AF demagnetization step. (Numbers in parentheses are meters sub-bottom.)

Table 1. Remanent magnetization of selected sediment samples after stepwise AF demagnetization.

Hole	Core	Section	Interval (cm)	Sub-bottom Depth (m)	AF Demag. Field (Oe)	Relative Declination	Inclination	Intensity ($\times 10^{-6}$ emu/cc)	Remarks
487	3	4	52.0–54.0	15.53	0	59.2	67.4	5.81	Type A
					50	32.8	48.9	2.54	
					100	54.2	71.5	3.06	
					150	56.9	78.6	3.24	
					200	41.3	74.9	4.14	
	14	2	100.0–102.0	117.51	0	116.4	35.3	5.39	Type A
					50	154.0	−10.1	2.25	
					100	165.7	−32.9	0.73	
					150	166.3	−26.5	0.73	
	19	2	16.0–18.0	164.17	0	132.2	−0.1	2.83	Type A
					50	162.7	−19.2	2.89	
					100	181.2	−30.9	3.40	
					150	181.2	−32.3	2.94	
					200	181.5	−36.3	2.66	
488	2	1	109.0–111.0	2.10	0	302.1	−20.8	58.16	Type T
					50	302.0	−19.6	58.01	
					100	299.8	−20.1	52.84	
					150	294.0	−18.6	43.95	
					200	290.9	−19.3	37.83	
					250	286.3	−20.3	32.36	
	31	3	131.0–133.0	280.32	0	223.0	−46.5	0.21	Type T
					50	228.0	−50.4	0.23	
					100	222.2	−58.4	0.24	
					150	227.2	−46.4	1.14	
					200	230.2	−54.8	1.07	
					250	234.8	−68.5	0.25	
489	1	4	47.0–49.0	4.98	0	79.7	48.6	7.22	Type I
					50	69.9	46.8	5.71	
					100	46.7	9.4	1.34	
					150	5.8	6.5	0.56	
					200	1.6	27.3	0.31	
	2	5	96.0–98.0	12.97	0	65.1	31.8	0.44	Type P'
					50	43.1	−3.9	0.23	
					100	34.5	3.7	0.21	
					150	22.1	−2.7	0.10	
					200	119.5	−25.2	0.03	
489A	23	5	132.0–134.0	224.33	0	151.4	1.3	0.327	Type I
					50	135.3	9.1	0.216	
					100	165.6	−24.0	0.167	
					150	139.5	−54.4	0.177	
					200	122.8	−38.1	0.117	
490	1	4	95.0–97.0	5.46	0	295.6	65.1	0.315	Type G
					50	280.5	−7.9	0.161	
					100	298.4	14.8	0.157	
					150	320.8	−33.4	0.194	
					200	331.4	−56.9	0.222	
	28	5	142.0–144.0	263.43	0	112.8	51.1	2.518	Type G
					50	109.9	50.7	2.101	
					100	108.9	47.7	1.816	
					150	112.8	29.1	1.678	
					200	106.6	47.1	1.539	
	64	1	146.0–148.0	580.47	0	323.4	27.5	1.662	Type S
					50	328.6	21.2	1.148	
					100	336.1	11.2	0.804	
					150	334.1	14.6	0.584	
					200	339.1	11.7	0.475	
491	10	5	127.0–129.0	93.28	0	79.2	64.1	10.069	Type T
					50	78.9	65.2	9.506	
					100	81.1	61.8	8.619	
					150	87.6	58.1	7.587	
					200	86.4	57.7	8.028	
	57	3	145.0–147.0	517.96	0	7.0	−12.0	15.213	Type T
					50	7.9	−13.0	15.435	
					100	6.6	−12.5	15.226	
					150	6.6	−12.4	15.327	
					200	8.7	−14.3	14.854	
492	2	4	94.0–96.0	8.95	0	133.2	20.4	0.506	Type P
					50	116.7	34.9	0.374	
					100	121.9	24.3	0.225	
					150	115.1	16.6	0.367	
					200	129.2	−18.3	0.244	
					250	125.7	−3.3	0.297	
	12	5	123.0–125.0	105.74	0	195.2	24.3	0.233	Type P
					50	227.8	27.5	0.173	
					100	247.3	26.2	0.097	
					150	230.2	25.9	0.110	
					200	275.9	14.2	0.109	
	25	5	101.0–103.0	229.02	0	174.6	24.9	1.923	Type T
					50	175.0	30.0	1.353	
					100	189.3	30.1	1.713	
					150	187.3	25.1	1.529	
					200	194.5	33.8	1.461	
492A	4	2	9.0–11.0	20.10	0	280.6	−11.8	0.158	Type G
					50	299.5	7.8	0.369	
					100	297.5	17.3	0.288	
					150	264.9	−28.1	0.163	
					200	281.6	11.1	0.208	
	6	1	68.0–70.0	28.69	0	27.1	40.2	0.653	Type S
					50	38.5	36.3	0.447	
					100	41.2	37.9	0.361	
					150	9.3	31.3	0.275	
					200	26.8	30.8	0.269	

Table 1. (Continued).

Hole	Core	Section	Interval (cm)	Sub-bottom Depth (m)	AF Demag. Field (Oe)	Relative Declination	Inclination	Intensity ($\times 10^{-6}$ emu/cc)	Remarks
493	14	5	92.0–94.0	240.93	0	17.1	74.1	0.255	Type S
					50	47.0	49.4	0.169	
					100	8.7	34.7	0.107	
					150	347.2	19.6	0.179	
					200	55.7	−46.6	0.126	
	30	5	78.0–80.0	392.79	0	78.8	69.2	1.241	Type S
					50	67.0	54.4	0.621	
					100	93.9	69.1	0.466	
					150	110.4	66.9	0.374	
					200	146.5	51.6	0.327	
	34	4	66.0–68.0	429.17	0	251.6	46.6	0.837	Type S
					50	252.2	41.6	0.775	
					100	253.4	49.4	0.491	
					150	249.0	46.0	0.281	
					200	236.8	55.6	0.134	
	54	3	64.0–66.0	617.65	0	154.4	60.4	0.055	Type I
					50	117.4	24.1	0.017	
					100	257.5	68.9	0.025	
					150	137.5	29.4	0.070	
					200	148.2	−19.6	0.047	

150 Oe the direction change is minimum—less than 7°. The remanent magnetization after 150-Oe AF demagnetization represents reliable paleomagnetic data.

Type I. This type occurs in muddy silt and muddy siltstone samples from the upper slope at Sites 489 and 493. Change in direction reaches a peak of more than 40° at 100 and 150 Oe. Intensity ranges from 2×10^{-8} to 7×10^{-6} emu/cc. This type of direction change is also found in ilmenite-rich plutonic rock from Site 493. For the paleomagnetic study, 150-Oe AF demagnetization is necessary to this type.

Type P′. This type occurs in mud samples from the upper slope at Sites 489 and 493. Direction change in AF demagnetization is more than 40°; the minimum change occurs at 100 and 150 Oe. At 200 Oe the amount of direction change is more than 90°. The reaction of remanent magnetization to AF demagnetization is similar to Type P but is twice the amount of direction change for Type P.

Remanent magnetization of samples from the lower slope and outer rise is generally stable and reliable. Some samples from the upper slope have less reliable remanent magnetization. Most of the soft component of remanent magnetization was eliminated effectively by 150-Oe AF demagnetization. In routine measurement of remanent magnetization, all paleomagnetic samples were measured after 150-Oe AF demagnetization. Because the types of reaction of remanent magnetization correlate well with magnetic mineral composition and sedimentary facies, they are useful for determining the origin of the sediments. The contrast in AF demagnetization between lower and upper slopes indicates different origins for the sediments.

Normal-Reverse Test

Inquiry into the reliability of remanent magnetization of sediments is possible also by normal–reverse, folding, slumping, conglomerate, and other tests. The normal-reverse test is applied to the sediment section accumulated during a period of geomagnetic polarity reversal or reversals. If the magnetic sequence includes both normal and reversed directions, the remanent magnetization is probably reliable.

Because with cored sediments we cannot determine the rotation angle of sediments around the drilling axis, inclination only is the basis of geomagnetic polarity determination. We cannot detect directly the effect of drilling disturbance on the remanent magnetization. A single core drilled at Site 488 comprises two positive intervals and one negative interval in inclination of remanent magnetization. In the upper two intervals, even though downward concave laminations along core tube margins indicate drilling disturbance, the sediments themselves did not appear to have been rotated. Figure 3 and Table 8 show the magnetic measurement of samples from these three intervals. Among them, changes in inclination to the opposite hemisphere are accompanied by those in declination of about 180°, which indicates that the sediment core recorded reversals of geomagnetic field and that the drilling disturbance did not affect the remanent magnetization and the inclination.

In the lower interval the sediment core is broken into pieces several centimeters thick which were rotated with respect to one another. In this interval the inclination changes gradually with the increase of subdepth from negative to positive and then to negative, though the apparent declination of samples was scattered (Fig. 4 and Table 8). Because the remanent magnetization of separated pieces was not affected by drilling disturbance, the inclination can be used to determine magnetic polarity.

In the upper part of Hole 492, Core 1, change in inclination accompanied that in declination of about 180° (Fig. 5 and Table 12), indicating reliability of the remanent magnetization.

Inclination Analysis

In this study, only the inclination of remanent magnetization is essential, because drilling rotated the samples. Because the bedding plane dips up to 74° in the Leg 66 area, the term *inclination* is used for the inclination after bedding correction.

Figure 6 is a histogram of the inclination of 541 sediment samples from the Leg 66 sites after AF demagnetization at 150 Oe. The histogram has bimodal distribution with peaks at positive and negative inclination
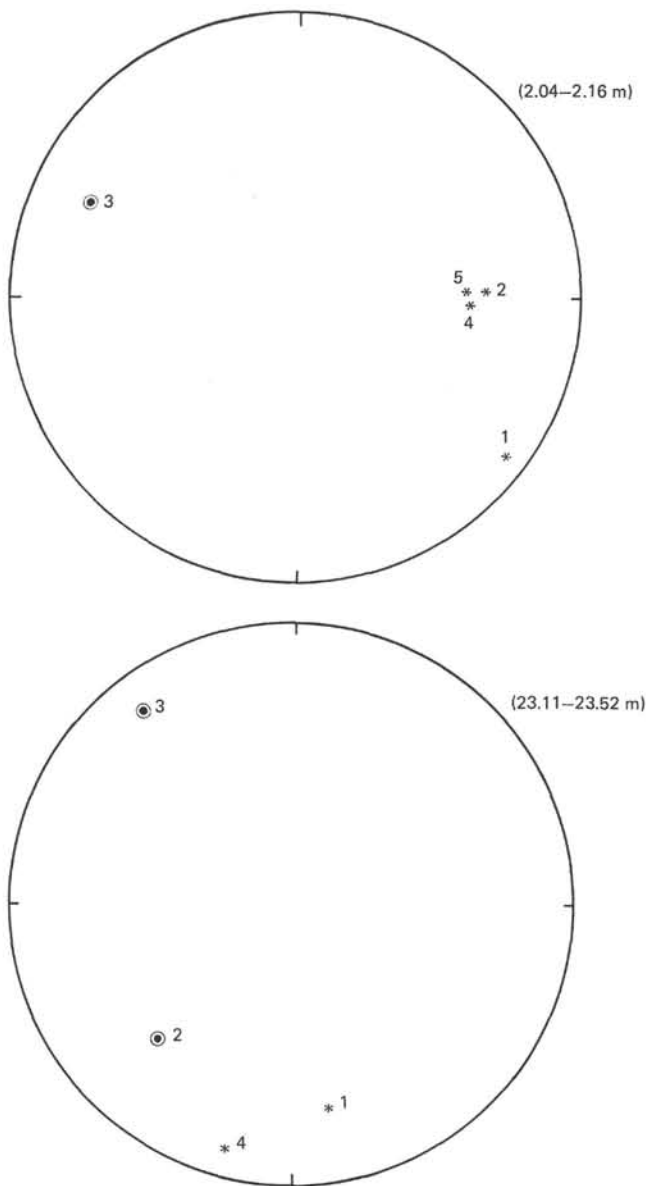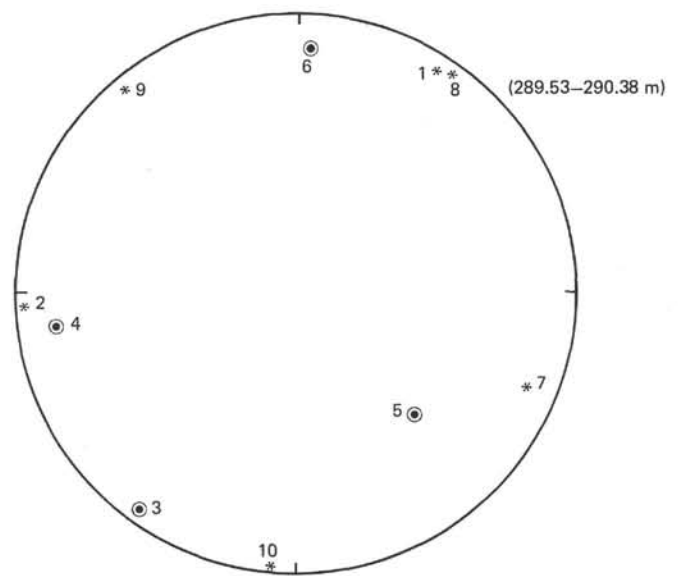
(2.04–2.16 m)

(289.53–290.38 m)

Figure 4. Normal–reverse test of lower part of Site 488 sediments. No systematic relation exists between inclination and declination. (Symbols as in Fig. 3.)
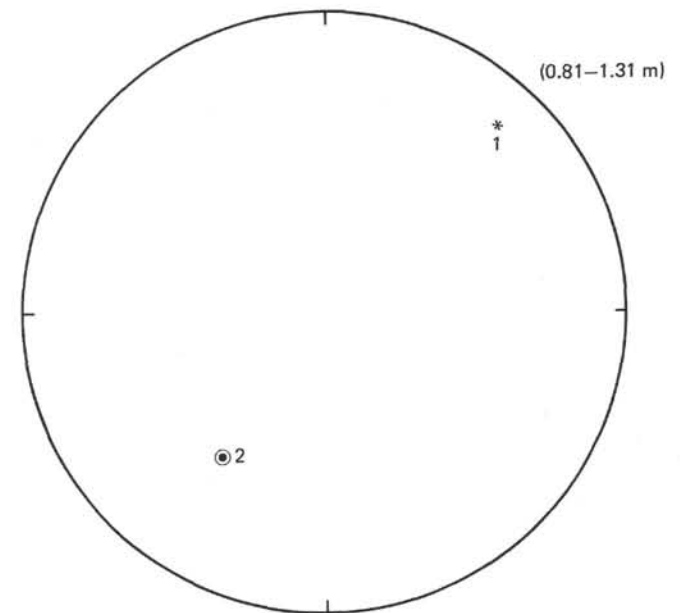

(23.11–23.52 m)

Figure 3. Normal–reverse test of upper part of Site 488 sediments. Inclination and relative declination are projected on stereo net. (• = upper hemisphere, * = lower hemisphere. Sample horizons are numbered from shallowest to deepest.)

(0.81–1.31 m)

Figure 5. Normal–reverse test of upper part of Site 492 sediments. (Symbols as in Fig. 3.)

and a gentle trough in the low inclination range between the two peaks.

Four factors control the inclination measurement: magnetic field direction during deposition, error in magnetization of sediments, overprint of remanent magnetization, and magnetometer noise. Magnetic field direction is related to latitude of the site, magnetic dipole position, and the nondipole component of the geomagnetic field. If the poles of the geomagnetic dipole locate on the earth's rotation axis (theoretical axial geocentric dipole), inclination should be 29.8° in the Leg 66 area at latitude 16°N. On the basis of the present pole position of the geomagnetic field (78.6°N, 69.8°W), the inclination is estimated as 44°. The actual inclination value is 40°, which is affected partly by the nondipole moment

of the geomagnetic field. Considering these components of the geomagnetic field, we can estimate that the inclination value has a dispersion within a range of 15° from 30° in this area.

Error in magnetization is likely in a random direction, and the inclination measurement includes a value randomly scattered by the error, especially in the case of sediments poor in magnetic minerals. Overprint of remanent magnetization correlates with the direction of magnetic field in which samples have been preserved after initial magnetization. If the overprint due to the
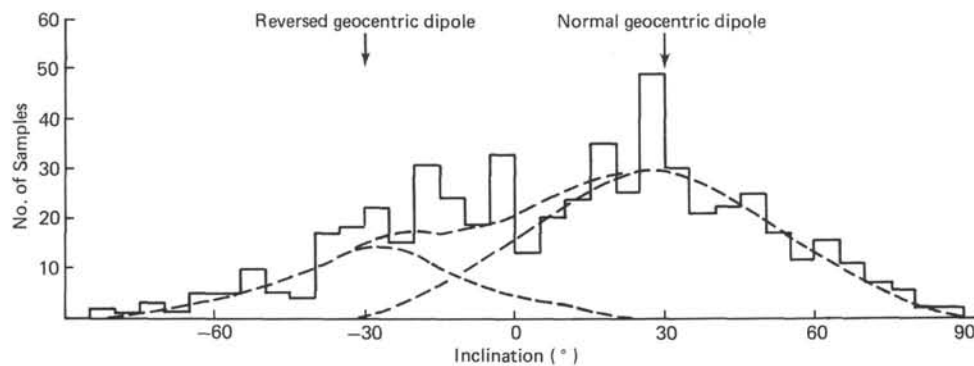
Figure 6. Histogram of inclination of sediment samples. Broken lines are best-fit normal distributions for the inclination data.

present magnetic field is dominant, the inclination should be positive. We can estimate the amount and character of the overprinted component by a demagnetization test. The overprint can be largely eliminated by AF demagnetization at 150 Oe. Magnetometer noise causes the inclination measurement to scatter, and the amount of dispersion should relate directly to the intensity of remanent magnetization in the sample.

In further analysis of inclination, I will use the following simple model. A certain average direction of magnetic field attributable to geocentric dipole and nondipole fields has lasted for one polarity interval—that is, long enough for accumulating sediments to acquire the remanent magnetization—then polarity reversed and the field direction lasted as long as before; finally, the event repeated itself in the same order. Throughout this process other factors randomly affected the inclination of remanent magnetization of the sediments. These factors comprise those dependent on and independent of magnetization intensity. Magnetic noise during measurement and magnetization error in sediments with fewer magnetic minerals are dependent on intensity. In my model, the frequency of inclination values has a bimodal distribution with maximum values at negative and positive inclinations corresponding to normal and reversed polarities, respectively; each maximum represents that of normal distribution of frequency of the corresponding polarity. At low latitude, as in the present area, the two normal distributions overlap, and a combination occurs in the frequency of inclination between the two modes—probably in low inclination intervals.

Inclinations of remanent magnetization in Leg 66 samples satisfy the aforementioned model. The average inclination value is 27.6°, calculated from cumulative frequency distribution of samples with various absolute inclination. This value agrees well with the theoretical inclination of 29.8°, and the average inclination of geomagnetic field in this area can be explained by the presence of geocentric dipole field during accumulation of the sediments.

From the frequency distribution of the inclination value corresponding to various intensities of remanent magnetization, we can estimate the relative importance of two random factors. Dispersion by randomness can

be represented as standard deviation calculated from frequency distribution corresponding to absolute inclinations larger than 30° (Table 2). There is no systematic change to be found in the standard deviation within the range of 10^{-8} to 10^{-5} emu/cc for remanent magnetization intensity. This fact indicates that the factor dependent on intensity is relatively small and should be of the order of 10^{-8} emu/cc in intensity. Probably most dispersion (at least 70%, or 15° in inclination) is the result of past changes in the geomagnetic field.

Using the average value and dispersion, we can calculate a frequency distribution of inclination in the interval from $-30°$ to $30°$. Distribution agrees well with the actual data (Fig. 6).

The standard deviation (23.6° for positive and 21.0° for negative inclination peaks) provides an estimate of the reliability of polarity determined by inclination. If we determine the polarity using only the sign of inclination—normal polarity from positive inclination and reversed polarity from negative inclination—the reliability of the determination is 87.9% for normal polarity and 90.5% for reversed polarity.

MAGNETIC PROPERTIES OF BASEMENT ROCKS

Reaction of remanent magnetization to AF demagnetization, changes in saturation magnetization (Js) with temperature (T), and magnetic properties of opaque minerals were examined in three ocean basalt, four metamorphic, and five plutonic rock samples from Holes 487, 489A, and 493, respectively.

Table 2. Standard deviation (σ) of inclination values for positive and negative modes of samples with different intensity ranges of remanent magnetizations, calculated for inclinations in absolute ranges larger than 30°.

Intensity Range of Samples	Positive Mode σ (N)	Negative Mode σ (N)
10^{-4}–10^{-5} emu/cc	20.2 (21)	— (2)
10^{-5}–10^{-6}	24.3 (37)	12.0 (19)
10^{-6}–10^{-7}	24.1 (73)	21.7 (28)
10^{-7}–10^{-8}	24.7 (33)	24.8 (19)
10^{-8}–10^{-9}	23.5 (7)	— (3)
Total	23.6 (171)	21.0 (71)

Ocean Basalts

Three samples were taken from the largest pieces of basalt recovered in Core 20 (Pieces 2, 13, 17) in Hole 487. Piece 2 was the only one large enough to have avoided drilling rotation. The intensity of magnetization is strong: Average and standard deviation are $10^{-2.43 \pm 0.10}$ emu/cc. Magnetization is also relatively hard, so that the direction of magnetization changed less than 5° by AF demagnetization. The intensity of remanent magnetization of the basalts decreases monotonously in stepwise AF demagnetization (Table 3 and Fig. 8). A ratio of intensity after AF demagnetization at 400 Oe against natural remanent magnetization evaluates the decrease by AF demagnetization. A higher ratio means a harder remanent magnetization. Among the three pieces, #13 has the highest ratio (0.75) and #17 the lowest (0.42) (Table 4).

Under the reflective microscope, opaque minerals in the basalt are of two kinds and are in the shape of magnetite. One is skeletal and the other cubic in shape (Plate 1, Figs. 1 and 4). The skeletal shape is similar to the shape of fish debris. The magnetite grains in the basalt have an almost skeletal shape, up to 30 μm long and 2 μm wide, and there is intense maghemitization in all grains. In large, cubic magnetite grains, it appears along the rim. In the three samples, magnetite grains are smallest in Piece 13 (< 7 μm) and largest in Piece 17 (up to 30 μm) (Plate 1, Figs. 2 and 3). The difference in size of magnetite in the basalts agrees with that in decrease of remanent magnetization by AF demagnetization, the smaller size corresponding to the higher ratio of $J_{400}/$ NRM. This relation can be explained by the fact that the remanent magnetization of large grain with magnetic multidomain structure is easily demagnetized by AF demagnetization.

Js–T curves of the three basalt samples are irreversible (Fig. 7). The magnetization Js decreases with increasing temperature (T) to a minimum value at a temperature of 355° to 360°C (T_{c1}), increases for a time, then decreases by further heating until magnetization is finally lost at temperatures of 570° to 580°C (T_{c2}). During the heating from T_{c2} to 650° to 750°C, no changes occurred in Js. In the cooling cycle Js started to increase at a lower temperature (T_{c3}) than T_{c2}. In this case T_{c2} corresponds to the breakdown temperature of titanomaghemite and T_{c3} to the Curie temperature of low-Ti spinel. The first decrease in magnetization Js in the heating cycle (T_{c1}) corresponds to the Curie temperature of original titanomagnetite and the minimum magnetization is caused by titanomaghemite. The peak at higher temperature can be explained as titanomaghemite undergoing a two-phase inversion to low-Ti spinel plus hemoilmenite. The Js after cooling to room temperature (J_{ho}) is several times larger than original magnetization (J_o). The higher value of the ratio J_{ho}/J_o means more intense titanomaghemitization of titanomagnetite grains. Among the samples, the ratio of Piece 13 was the highest and that of Piece 17 the lowest (Table 4). The higher ratio corresponds to the finer grain size of titanomagnetite. This relation between ratio and grain size indicates that the titanomagnetite has been oxidized from the surface of grains inside and altered to titanomaghemite, because the finer grains have a relatively larger surface area.

Ulvospinel content in original titanomagnetite is estimated as 35 mol.% at the Curie temperature (T_{c1}), using the relation of Akimoto (1962). The content of ulvospinel in the titanomagnetite is consistent with the results of electron microprobe analysis of the present samples—31–39 mol.% (Arai, this volume). An ulvospinel content of 35% is remarkably smaller than the $62 \pm 4\%$, of average and standard deviation of ulvospinel in submarine basalts reviewed by Johnson (1979).

The inclination of the largest piece of basalt is $-28.8 \pm 0.2°$, which agrees fairly well with the inclination of reversed axial geocentric dipole ($-29.6°$) in the latitude of this site (15.9°N). Site 487 is on the northeastern margin of a positive anomaly crest with an amplitude of 50 nT (Shipley et al., 1980). Although the data on the marine magnetic anomaly and the direction of remanent magnetization of oceanic basement in this area are insufficient to discuss the source of anomaly, the magnetic intensity of basalt is strong enough to make an anomaly.

Metamorphic Rocks

We took five metamorphic rock samples from Cores 33 and 34 in Hole 489A in the upper slope. The metamorphic rocks are schist with biotite-hornblende-quartz, garnet-muscovite-quartz, and biotite-muscovite-quartz associations and muscovite-chlorite-bearing quartzite. Average and standard deviation of natural remanent magnetization intensity of the metamorphic rocks is $10^{-6.9 \pm 0.5}$ emu/cc. Behavior of remanent magnetization to stepwise AF demagnetization is shown in Figure 8 and listed in Table 3. Three of the samples evidence different behaviors from each other. The sample from 309.21 meters subdepth has small changes in direction at 150- and 250-Oe AF demagnetization and almost constant intensity. The sample from 309.61 meters subdepth changes up to 40° in direction at 100 and 150 Oe—characteristic behavior for Type I magnetization of sediments mentioned earlier—and has gradually increasing intensity. The sample from 318.06 meters subdepth changes direction by more than 120° at 200 Oe—characteristic behavior for Type P magnetization of sediments—and has increasing intensity from a minimum value at the 150-Oe step.

Under the reflective microscope, we saw very small amounts of opaque mineral in the metamorphic rocks. These minerals are associated with mafic minerals. They are predominantly oxide minerals and crack-filling pyrite, though pyrrhotite and chalcopyrite are occasionally present. The oxide minerals are lath-shaped ilmenite and rutile (Table 5). The oxide mineral lath is 30 to 100 μm long and a 20 to 30 μm across (Plate 1, Fig. 5).

The Js–T curve of the metamorphic rocks gave no information owing to their low magnetic mineral content.

The weak remanent magnetization of the metamorphic rock in Hole 489A is inconsistent with the magnetic

Table 3. Remanent magnetization of basement rocks after stepwise AF demagnetization.

Hole	Core	Section	Interval (cm)	Sub-bottom Depth (m)	AF Demag. Field (Oe)	Relative Declination	Inclination	Intensity ($\times 10^{-6}$ emu/cc)	Susceptibility ($\times 10^{-6}$ cgs)	Remarks
487	20	1	9.0–11.0	172.10	0	85.7	−28.7	2870.0	196	Basalt
					50	85.1	−28.5	2830.0		
					100	85.1	−28.8	2670.0		
					200	85.9	−28.7	2480.0		
					300	86.2	−28.9	2230.0		
					400	84.5	−29.0	1950.0		
					500	84.5	−28.9	1670.0		
					600	84.2	−29.2	1420.0		
	20	1	93.0–95.0	172.94	0	288.7	−10.4	4170.0	324	
					200	288.7	−11.8	3820.0		
					400	289.4	−15.1	3130.0		
					600	290.3	−14.9	2320.0		
	20	1	118.0–120.0	173.19	0	52.3	6.3	4350.0	182	
					100	52.8	7.0	3720.0		
					200	53.1	7.3	3090.0		
					400	54.1	7.4	1840.0		
					600	54.5	6.7	1090.0		
489	33	1	20.0–22.0	309.21	0	251.7	−39.0	0.211		Metamorphic rock
					50	207.7	−39.5	0.197		
					100	179.1	−32.5	0.194		
					150	174.3	−19.9	0.249		
					200	147.0	−7.1	0.223		
					250	145.1	−16.6	0.199		
	33	1	28.0–30.0	309.29	0	171.2	−55.8	0.451		
	33	1	60.0–62.0	309.61	0	173.5	56.6	0.136		
					50	171.4	43.1	0.167		
					100	199.9	79.6	0.206		
					150	151.8	43.4	0.274		
					200	163.3	65.2	0.290		
					250	152.3	64.1	0.282		
	34	1	5.0–7.0	318.06	0	266.2	−24.8	0.169		
					50	276.6	−0.4	0.148		
					100	257.7	−7.7	0.134		
					150	229.0	−37.0	0.065		
					200	322.8	55.2	0.408		
					250	348.0	22.7	0.252		
	34	1	50.0–52.0	318.51	0	347.4	66.5	0.023		
493	58	1	52.0–54.0	652.53	0	206.5	67.6	79.416		Plutonic rock
					50	172.7	16.8	51.081		
					100	281.7	60.9	22.933		
					150	135.7	9.4	35.367		
					200	150.2	−7.3	45.463		
					300	246.6	23.8	38.143		
					400	55.9	13.5	38.231		
	58	1	59.0–61.0	652.60	0	216.3	65.1	82.742	122	
	58	1	73.0–75.0	652.74	0	50.5	50.2	2.247	64	
					50	57.6	43.3	1.855		
					100	67.5	8.9	1.366		
					150	350.6	20.2	0.996		
					200	0.2	0.3	1.061		
	59	1	137.0–139.0	657.88	0	258.5	68.2	18.680	54	
	59	2	74.0–76.0	658.75	0	174.7	64.9	455.667	168	
	60	1	79.0–81.0	662.80	0	148.2	57.5	6.354	52	
	60	2	39.0–41.0	663.40	0	142.2	72.4	1.774	68	

Table 4. Magnetic properties of ocean basalt, Hole 487, outer rise.

Core/ Section/Piece	Sub-bottom Depth (m)	T_{c1} (°C)	T_{c2} (°C)	T_{c3} (°C)	J_{ho}/J_o	J_{400} Oe/ J_{NRM}	Grain Size of Magnetite (μm)
20-1 2	172.10	360	565	545	4.69	0.68	5–10
20-1 13	172.94	355	570	545	4.79	0.75	2–10
20-1 17	173.19	355	570	532	2.53	0.43	4–20

anomaly of amplitude of 150 nT observed by Shipley et al. (1980).

Plutonic Rocks

The plutonic rocks recovered from Site 493 on the upper slope are diorite, of which seven oriented samples were used in this study. Intensity of natural remanent magnetization is widely scattered, average and standard deviation being $10^{-4.7 \pm 0.9}$ emu/cc. Susceptibility is
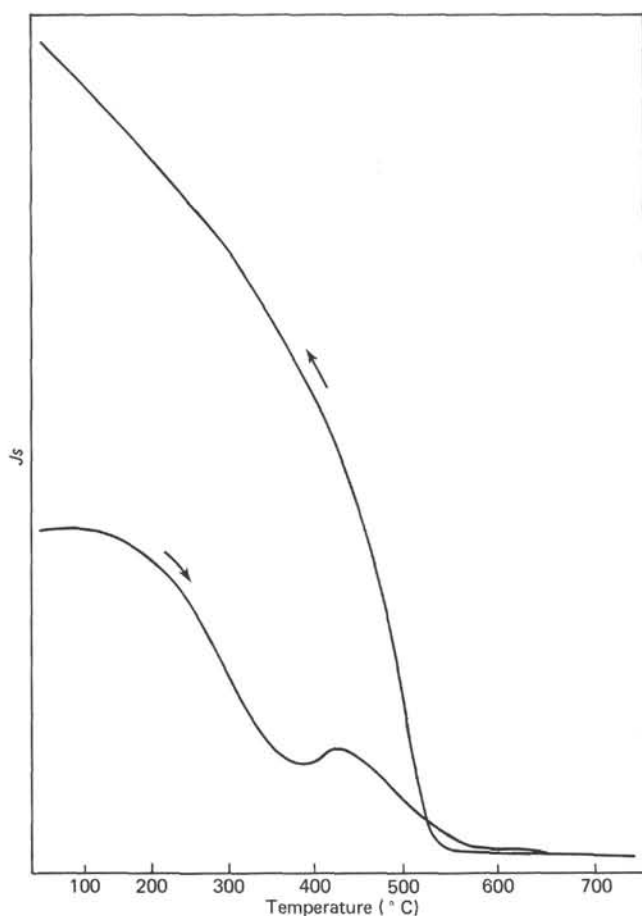
Figure 7. Saturation magnetization (*Js*)–temperature curves of ocean basalt, Section 487-20-1, Piece 17 (173.19 m sub-bottom).

$10^{-4.1 \pm 0.2}$ cgs. Inclination of natural remanent magnetization is $63.7 \pm 5°$, which is remarkably steep compared with that of axial dipole (29.8°). Remanent magnetization during AF demagnetization is unstable. Two samples from 652.7 and 653.0 meters subdepth were examined by stepwise AF demagnetization (Table 3). Both behave similarly: more than 70° change in direction of remanent magnetization at 150 Oe and generally decreasing intensity (Fig. 8). This behavior is similar to Type I for sediments.

Under the reflective microscope, the plutonic rocks were seen to contain predominantly ilmenite as oxide mineral, pyrite, pyrrhotite, and occasionally chalcopyrite as a sulfide mineral (Table 6). The opaque minerals are generally granular and range from 10 to 500 μm. Among the sulfide minerals, pyrite content is higher than pyrrhotite. There is twinned pyrrhotite, 200 μm across, in the sample from 658.75 meters subdepth, which has the strongest intensity of natural remanent magnetization among the plutonic rocks drilled. The composition of the opaque minerals indicates that the plutonic rock belongs to the "ilmenite series" of plutonic rocks (Ishihara, 1977), which are exposed on the circum-Pacific coasts.

Js-T curves of the plutonic rocks are irreversible. *Js* decreases gradually as temperature increases. At 520° to 560°C the sample weight decreases and remains constant up to 700°C. At temperature higher than 700°C, sample weight decreases gradually with increase of temperature. In the cooling cycle from 870°C, *Js* appears at the Curie temperature of 770°C and *Js* increases with cooling. *Js* at room temperature is larger than before heating (Fig. 9). Increased *Js* after heating means that magnetic material was produced during heating. The Curie temperature of the new material is 770°C, which is the same as metallic iron; therefore the new material is probably metallic iron produced by the reduction of iron sulfide, pyrite, pyrrhotite, and chalcopyrite. The *Js-T* curve of the sample from 658.75 meters subdepth is also irreversible. This sample has a Curie temperature of 320°C in the heating cycle and 270°C in the cooling cycle after heating to 600°C. The *Js* at room temperature after heating is smaller than before (Fig. 9). The change in Curie temperature and *Js* can be explained by a decrease in sulfur content in the pyrrhotite during heating. In this sample there is a decrease in weight at 540°C, as in the other plutonic samples, which is explained by decomposition of sulfide minerals.

It is difficult to identify these plutonic rocks as the source of the 150-nT marine magnetic anomaly in the upper slope area (Shipley et al., 1980), because the strongest intensity of the remanent magnetization in the plutonic rock is $10^{-3.34}$ emu/cc, one order weaker than the intensity of ocean basalt at Site 487. Steep positive inclination of natural remanent magnetization is probably caused by an induced magnetic field in the drilling core tube, judging from the direction of remanent magnetization and the unstable soft nature of remanent magnetization.

MAGNETOSTRATIGRAPHY

Magnetostratigraphy was established for the sedimentary sequences in the outer rise (Site 486), lower slope (Sites 488, 491, and 492), and upper slope (Sites 490, 489, and 493). The magnetic polarity was based mainly on the inclination of remanent magnetization after bedding correction, declination of nonrotated cores, and relative declination to dip of bedding plane, if data were available.

In the sequences of the upper slope, tectonic breaks due to faulting occur at a subdepth of 420 meters at Site 490, and sedimentary breaks occur at 5 to 7 meters at Site 489 and at 360 meters at Site 493, which is related to an unconformity. The tectonic break is suggested by the existence of many minor faults with slickensides and by the increased dips of bedding planes around the faults, soupy crashed sediments, and remarkably low recovery rate. The sedimentary breaks are identified by changes in color, hardness, and fossil content. The fossil data indicate ranges of hiatus in age from late early Miocene to Pleistocene at Site 489 and from late early Miocene to early late Miocene at Site 493.

Magnetostratigraphic correlation was based principally on the normal–reversed polarity sequence but was supplemented with nannoplankton and radiolarian fossil data (Stradner, this volume; McMillen, this volume). The units of magnetostratigraphic correlation are
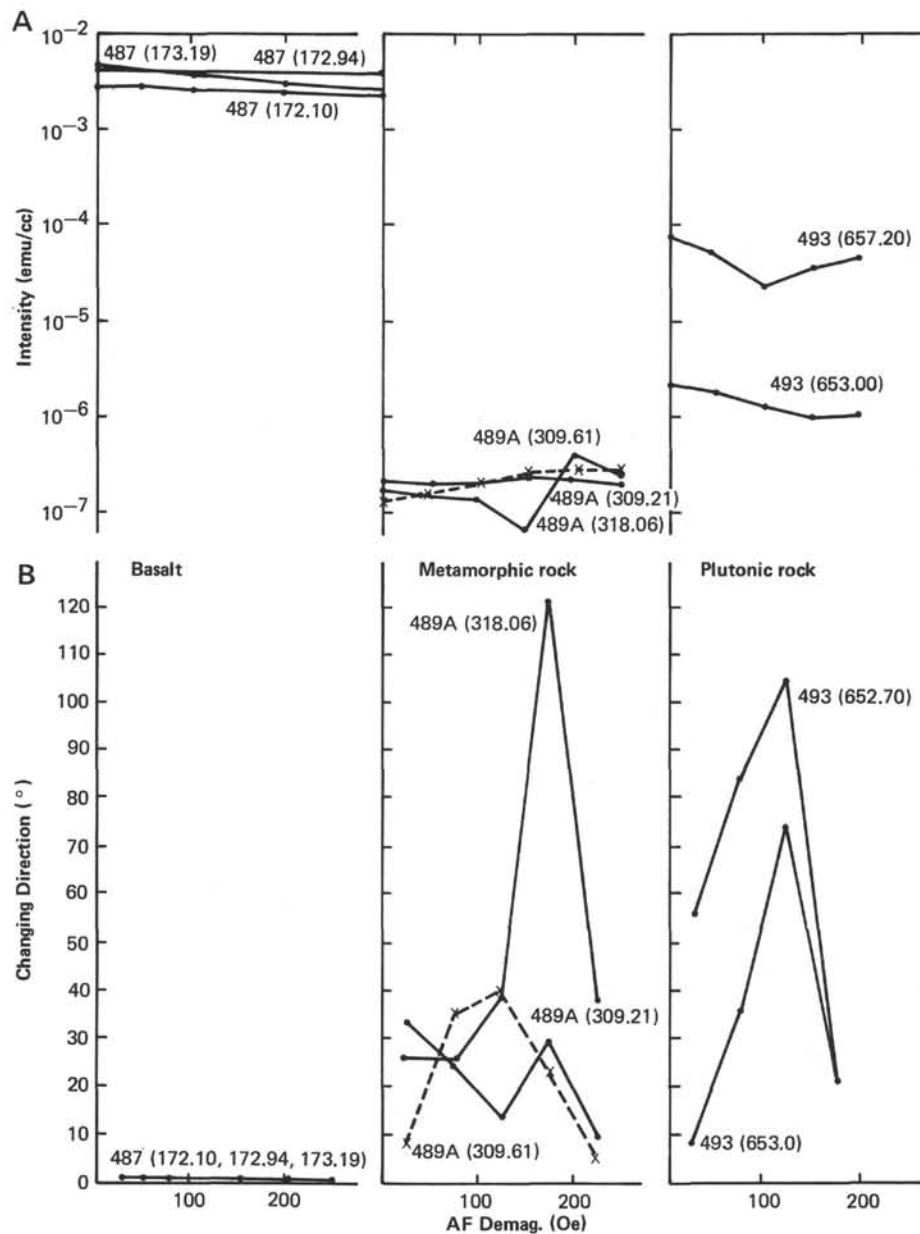
Figure 8. Reaction of remanent magnetization of basement rocks during stepwise AF demagnetization. A. Changes in intensity of remanent magnetization in a logarithmic scale. B. Changes in direction of remanent magnetization in degree with each AF demagnetization step. (Numbers in parentheses are meters sub-bottom.)

Table 5. Reflective minerals and magnetic properties in metamorphic rocks, Hole 489A, upper slope.

Core/Section	Sub-bottom Depth (m)	Reflective Mineral (size)	Remarks
33-1, 21 cm	309.21	Il, Rt (20μm) ≫ Py	Reflective mineral rare
33-1, 29 cm	309.29	Il, Rt (10–30, 100)	
33-1, 61 cm	309.61	Il(40) > Py(100) ≥ Rt(20)	Type I
34-1, 6 cm	318.06	Rt(30), Py(50–100) ≫ Il, Po, Cp	Type P

Note: Il = ilmenite, Rt = rutile, Py = pyrite, Po = pyrrhotite, Cp = chalcopyrite.

numbered starting with the youngest (Epochs 1 through 4 corresponding to the Brunhes, Matuyama, Gauss, and Gilbert polarity epochs and Epoch 5 below the Gilbert). The magnetostratigraphic columns and results of mea- surement are shown in Figures 10–17 and listed in Tables 7–13. Magnetostratigraphic correlation between the sites and comparison with a standard magnetostratigraphic scale (Ryan et al., 1974) are shown in Figure 18, together with the horizons of the pilot samples examined by stepwise AF demagnetization and their types.

Outer Rise

Hole 487. Remanent magnetization of samples from Hole 487 shows a relatively strong average intensity ($10^{-5.35 \pm 0.43}$ emu/cc) after 150-Oe AF demagnetization (Fig. 10). The magnetization is stable and all pilot samples belong to Type A (Fig. 18). The upper half of the sequence can be correlated with Brunhes Normal Polar-

Table 6. Reflective minerals in plutonic rocks at Site 493, upper slope.

Core/Section/Piece	Sub-bottom Depth (m)	Reflective Mineral (µm)	Remarks
58-1 5	652.70	Il(500) ≫ Py(20–100) > Po(10–50) ≫ Cp(10)	
59-2 9	658.75	Il > Po > Py > Cp	Granular, 20–500 µm
60-1 3	662.90	Il ≫ Py, Po ≫ Cp	Granular, 10–80 µm
60-2 4	663.40	Il(10–50) ≫ Py(10–150) > Po(10) ≫ Cp	

Note: Il = ilmenite, Py = pyrite, Po = pyrrhotite, Cp = chalcopyrite.
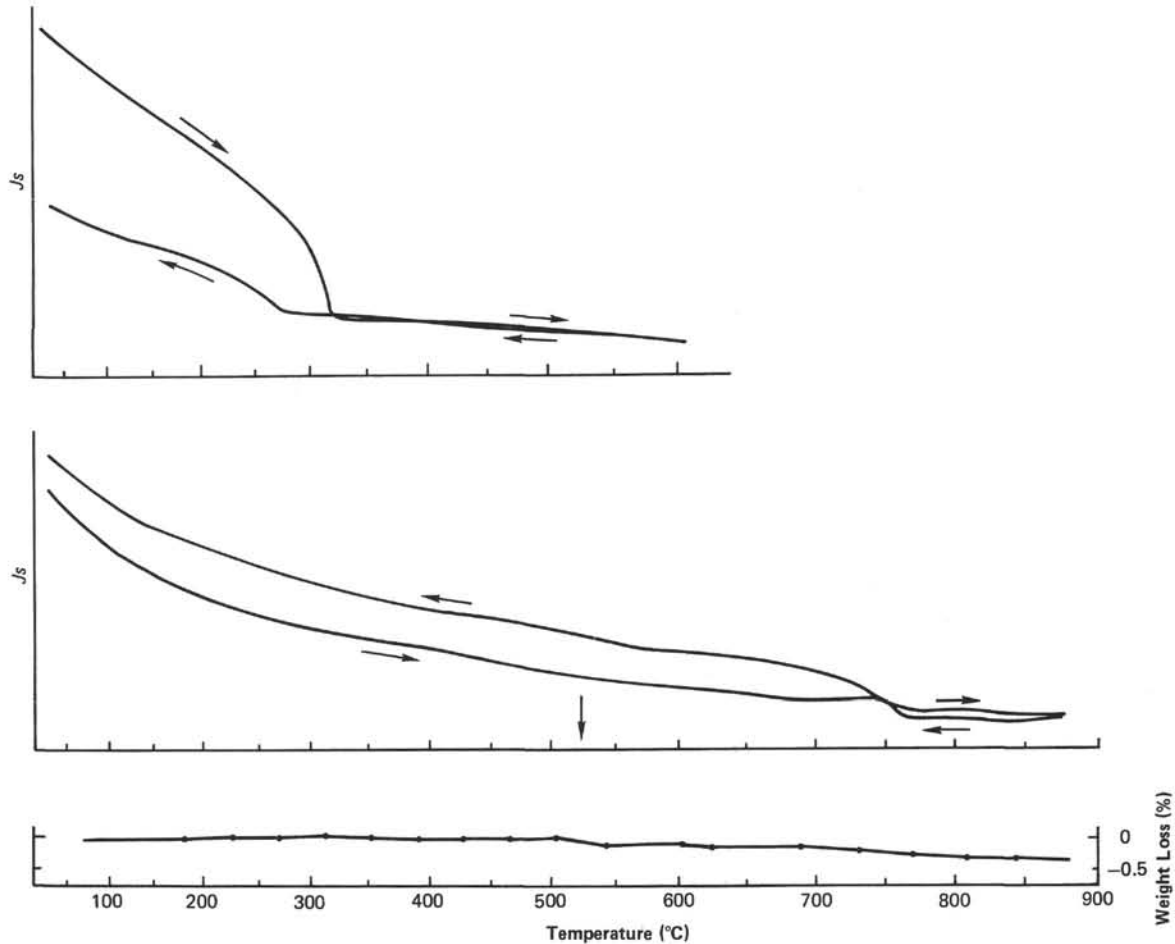
Figure 9. Saturation magnetization (*Js*)–temperature curves of plutonic rocks, Site 493, upper slope. (Top): Section 493-59-2, Piece 9 (658.75 m sub-bottom); (bottom): Section 493-60-1, Piece 3 (662.90 m sub-bottom).

ity Epoch and the lower half with the Matuyama Epoch through Epoch 10. The magnetostratigraphic correlation indicates a large increase in the rate of sedimentation in the last 0.69 m.y.

Lower Slope

Hole 488. The average intensity of remanent magnetization is $10^{-5.27 \pm 0.64}$ emu/cc after 150-Oe AF demagnetization (Fig. 11). The magnetization is stable and belongs to Type T. The magnetostratigraphic sequence is correlated with the Brunhes Epoch and the later part of the Matuyama Epoch, including Jaramillo Event. Short events at three horizons in the later part of the Brunhes Epoch and two horizons in late Matuyama Epoch are recognizable not only by inclination but by declination as well. Such short events have been reported in Lake Biwa sediments (late Brunhes Epoch) (Yaskawa et al., 1973).

Hole 491. The average intensity is $10^{-5.8 \pm 0.7}$ emu/cc after 150-Oe demagnetization (Fig. 14). The magnetization of the samples belongs to Type T, which has stable remanence direction. The magnetostratigraphic sequence is correlated with Epochs 1 through 4. Above 76 meters subdepth, intensity is remarkably low, ($10^{-6.7 \pm 0.7}$ emu/cc) and the rate of sedimentation is also low.

Hole 492. The average intensity is $10^{-6.6 \pm 0.6}$ emu/cc. This intensity is the same as in the upper part of Hole 491. The intensity of the lowest part, below 228 meters subdepth, is $10^{-5.7 \pm 0.7}$ emu/cc, the same as at Site 488. The remanence of the upper part of the sediments at this site belongs to Type P and of the lower part to Type T. Because the sediments have been brecciated tectonically,
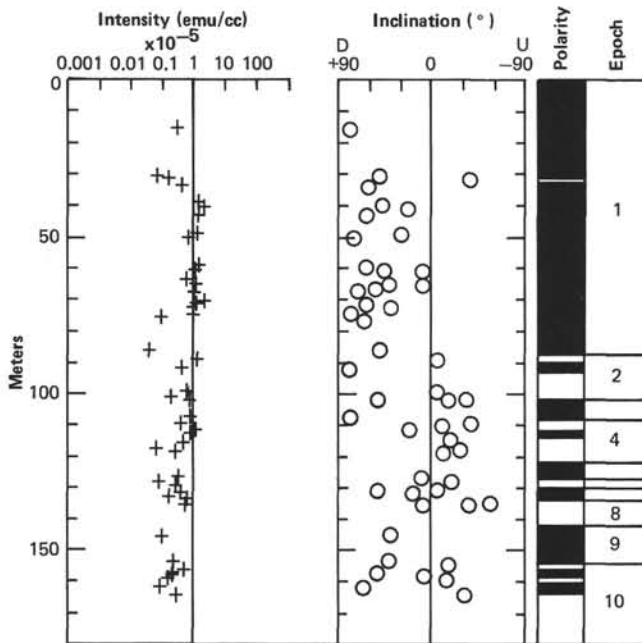
Figure 10. Magnetostratigraphy, Hole 487, outer rise.

no paleomagnetic sample was collected in the intervals from 125 to 155 meters or from 190 to 210 meters. The magnetostratigraphic sequence is correlated with Epochs 1 through 9.

Hole 492A. The average intensity is $10^{-6.5 \pm 0.3}$ emu/cc (Fig. 16). The sediments contain glauconite. The remanence is Type G. Normal polarity dominates the magnetostratigraphic sequence, of which correlation with Site 492 is difficult, because the upper parts of the sequences in Holes 492 and 492A may have hiatuses, and sediment accumulation not have been uniform.

Upper Slope

Hole 490. The average intensity of remanent magnetization is $10^{-6.6 \pm 0.9}$ emu/cc (Fig. 13). Type of remanence is S and G. The magnetostratigraphic sequence is correlated with Epochs 1 to 5 and indicates a uniform rate of sedimentation. A normal fault exists in the middle of Epoch 4 (= Gilbert Reversed Polarity Epoch). The correlation indicates that the missing interval ranges from 3.7 to 4.6 Ma (Events a through c_2).

Hole 489. The average intensity of remanent magnetization is $10^{-7.2 \pm 0.8}$ emu/cc, which is one to two orders lower than that of the other lower slope sites (Fig. 12). The magnetization is Types I and P. There is an unconformity in the uppermost part of the sequence, and the magnetostratigraphic sequence below the unconformity correlates with Epochs 17 through 21.

Hole 493. The average intensity is $10^{-6.8 \pm 0.5}$ emu/cc (Fig. 17). The samples from the upper 360 meters were demagnetized twice in an alternating field of opposite directions at 150 Oe to examine stability. The results are shown in Table 13 and Figure 17. Type of remanence is S and I. The sedimentary sequence is divided into two—upper and lower—by unconformity. The upper magnetostratigraphic sequence is correlated with Epochs 1
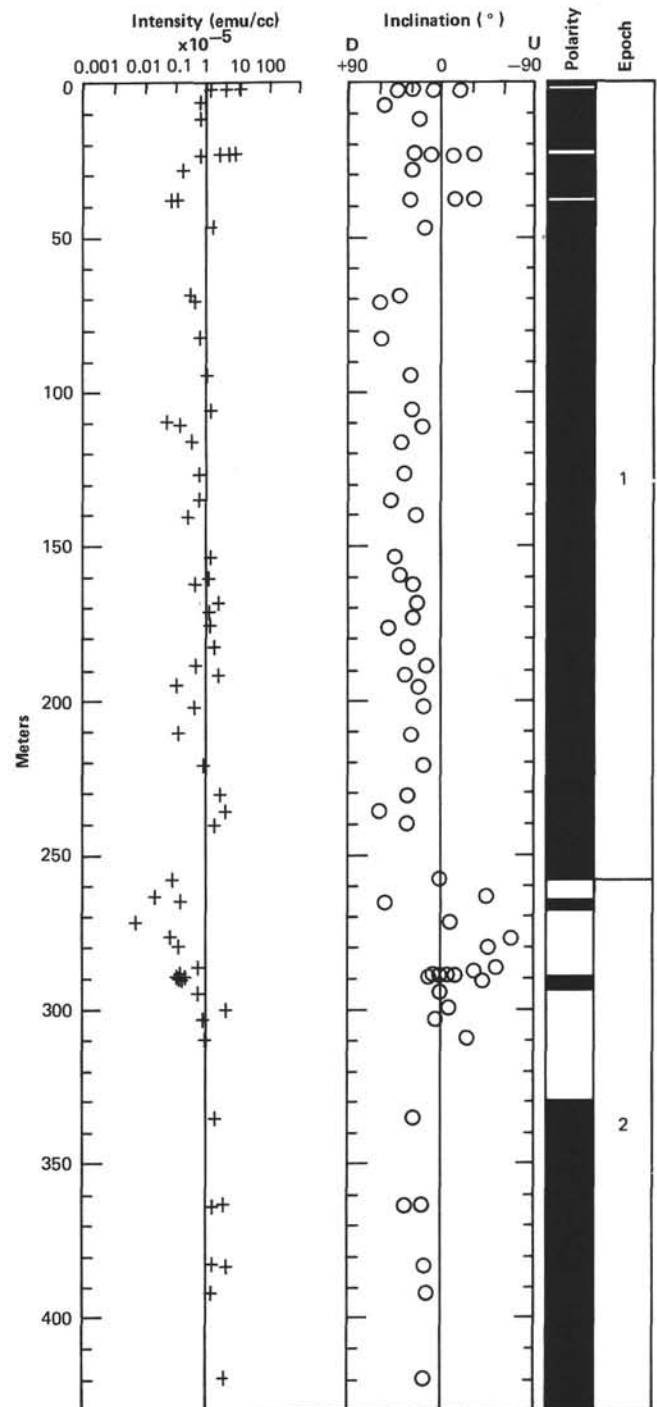
Figure 11. Magnetostratigraphy, Hole 488, lower slope.

through 8 and the lower sequence with Epochs 16 and 17. The hiatus represented by the unconformity extends from 8.5 to 18.0 Ma. Very little intensity difference is observed between the lower section of lower Miocene and the upper section of the upper Miocene to Pleistocene. This indicates that sediments with a similar magnetic mineral content have been supplied to the present area in the early Miocene and late Miocene to Pleistocene, probably from the same source area. The absolute inclination in the lower section ($42.9 \pm 20.7°$) is signifi-
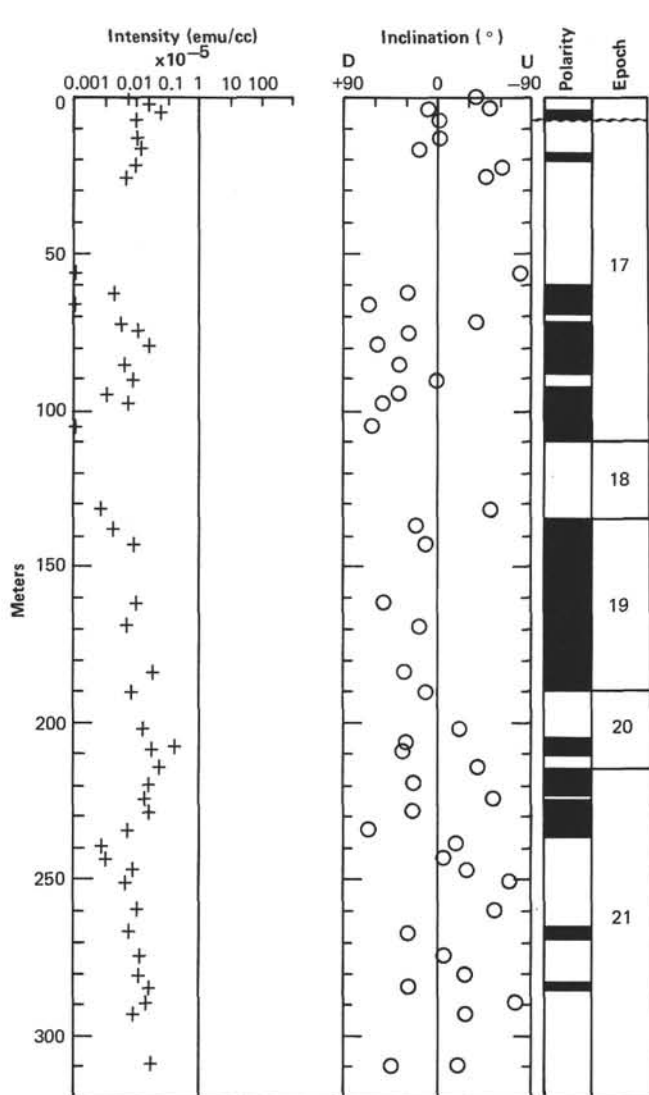
Figure 12. Magnetostratigraphy, Holes 489 and 489A, upper slope.

cantly larger than in the upper section (27.5 ± 21.2°), which agrees with the present geocentric axial dipole value. If the higher inclination is adopted, paleolatitude is calculated as 25.0° on the assumption that the average inclination represents a geocentric axial dipole during the early Miocene.

The intensity of remanent magnetization of the upper slope sediments is uniformly weak, and the sediments show reactions to AF demagnetization different from those of the lower slope and outer rise sediments. Thus the origin of the upper slope sediments may be different from that of the lower slope and outer rise sediments. The weak intensity and types of reaction to AF demagnetization are similar to the intensity and reactions of plutonic and metamorphic rocks from continental basement.

The most conspicuous characteristic of the sediment accumulation rate in the upper slope area is an unconformity in the middle Miocene (Fig. 18). The age of the sedimentary break ranges from the late early Miocene (16.5 Ma) to the middle late Miocene (8.5 Ma).
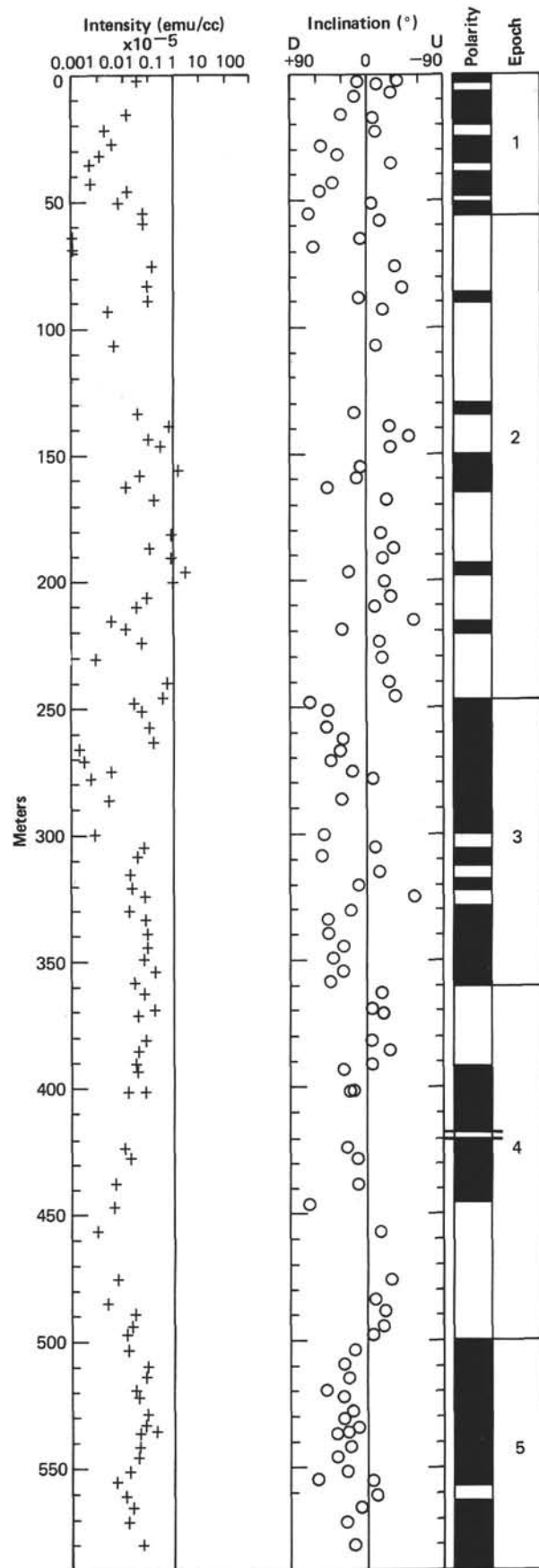
Figure 13. Magnetostratigraphy, Hole 490, upper slope.
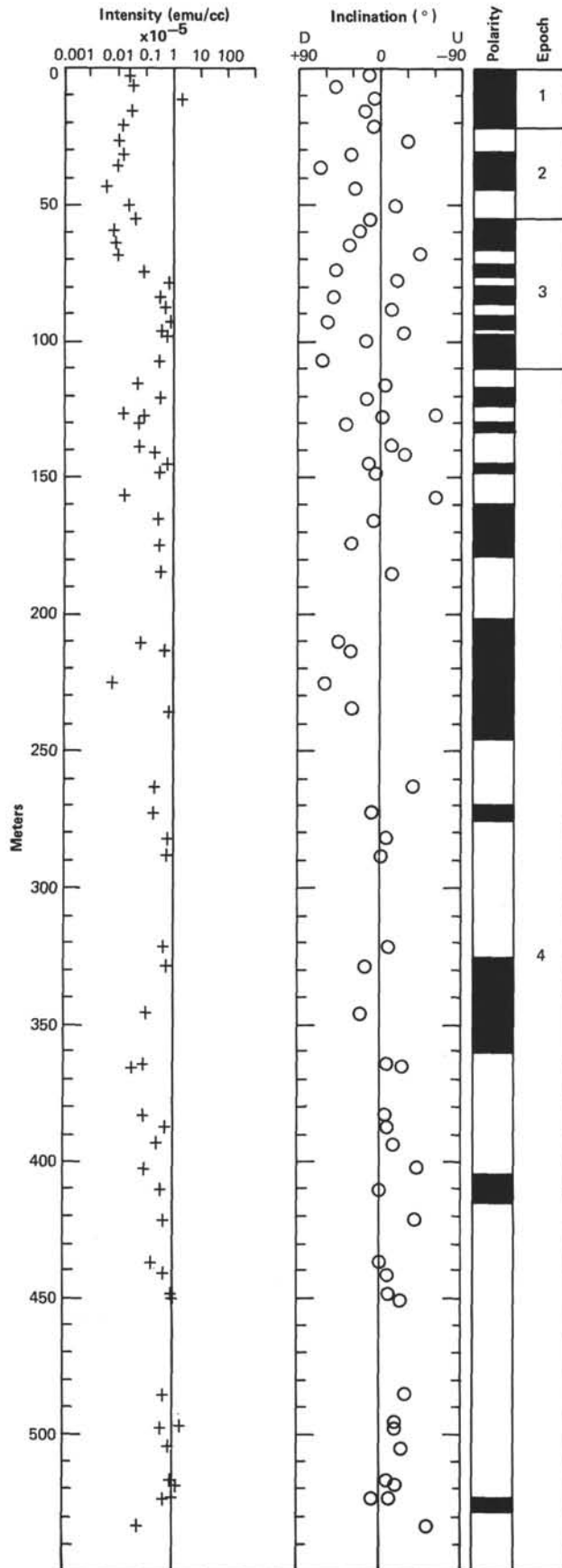
Figure 14. Magnetostratigraphy, Hole 491, lower slope.
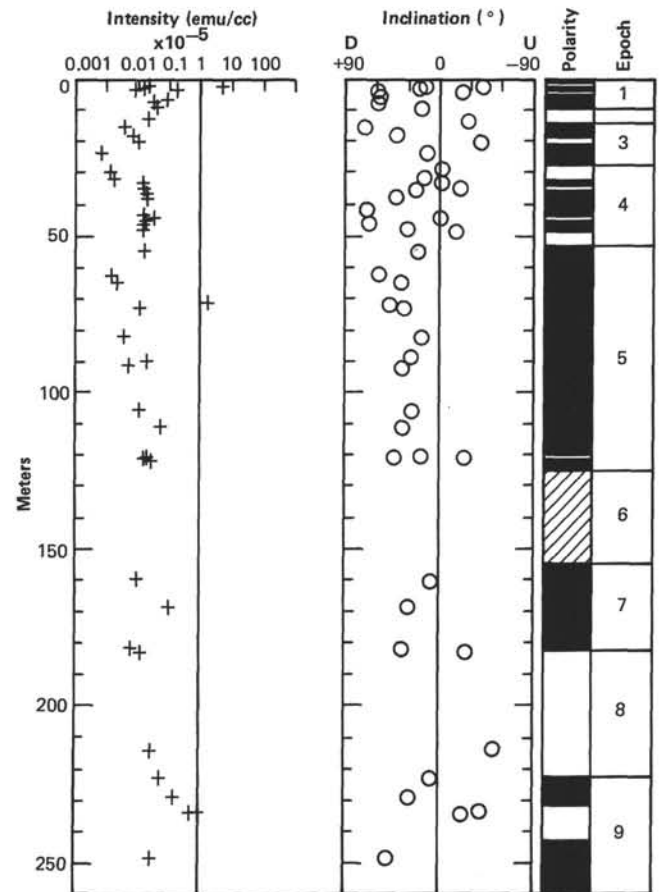
Figure 15. Magnetostratigraphy, Hole 492, lower slope.
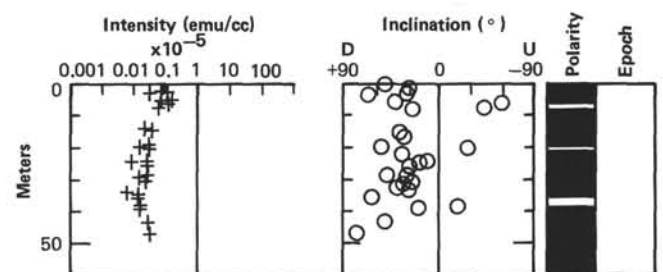
Figure 16. Magnetostratigraphy, Hole 492A, lower slope.

SEDIMENT ACCUMULATION ON THE LOWER SLOPE AND OUTER RISE DURING THE LAST 0.69 M.Y.

Rate of Sedimentation

There exists a clear relationship between rate of sedimentation and the distance of sites from the Middle America Trench (Fig. 19): the rate (paleomagnetically determined) of sedimentation during the last 0.69 m.y. (Brunhes Normal Polarity Epoch) in the lower slope area, Sites 488, 491, and 492, clearly decreases as distance from the trench increases (see also Shepard and McMillen, this volume).

751
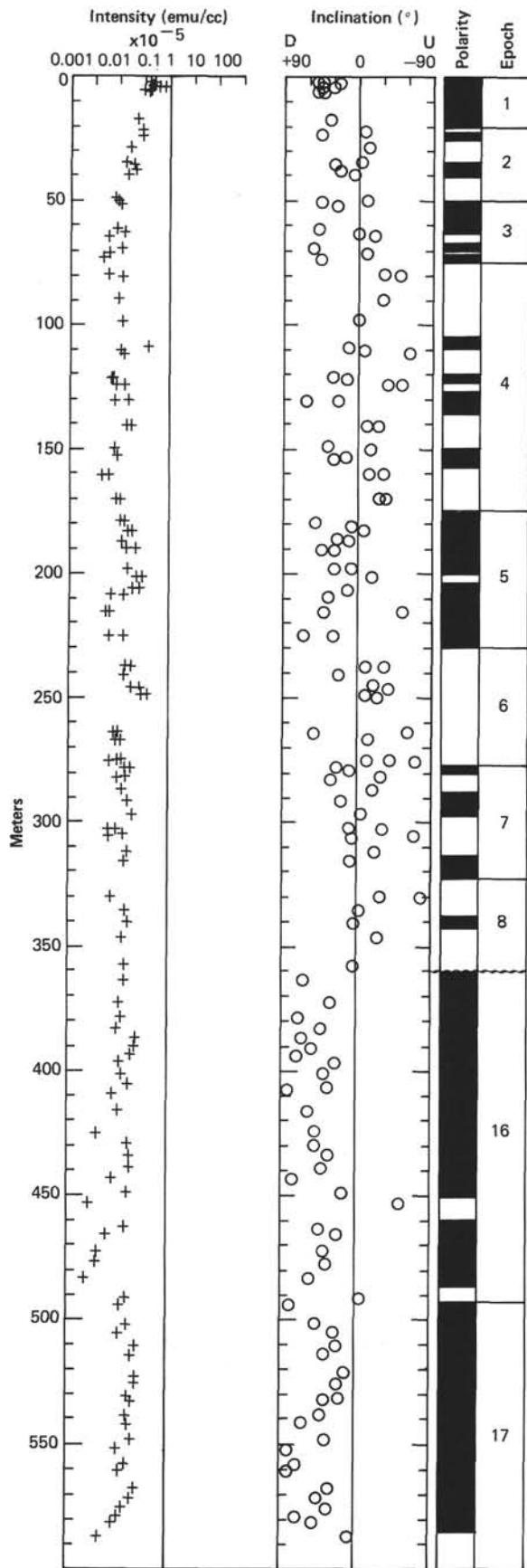
Figure 17. Magnetostratigraphy, Holes 493, 493A, and 493B, upper slope.

Site	Distance from the Trench (km)	Sedimentation Rate during Last 0.69 m.y. (m/m.y.)
488	6.6	374
491	16.7	31.9
492	22.8	14.8

Figure 19 shows that the rate of sedimentation in the lower slope area decreases exponentially with an increase in distance from the trench. The relation can be expressed by the following equation:

$$r = R e^{-k_s D}, \qquad (1)$$

where r is rate of sedimentation in m/m.y. at a given site at a distance of D (km) from the trench axis, R is a rate of sedimentation along the trench axis in m/m.y., and k_s is a constant. Using the data of the three sites, we obtain 0.21 as the value of k_s. This value means that the rate of sedimentation in the lower slope decreases one order of magnitude every 11.2 km of distance from the trench axis and the rate of sedimentation along the trench axis may be 1353 m/m.y.

We have to treat Site 487 in a somewhat different manner, because it is at the east end of the Cocos Plate. There is an interesting change in rate of sedimentation in the sequence at Site 487. The rate of sedimentation at 6.9 m/m.y. was almost constant before 0.89 Ma. Since then the rate increased rapidly to more than 127 m/m.y. This increase is probably related to the change in the relative location of Site 487 with respect to the Middle America Trench, the change being due to ocean floor spreading and subduction. I analyzed this increased rate, using the rate of Cocos Plate motion against that of the North American Plate and assuming that sedimentation rate decreases exponentially with increase in distance from the trench axis. Given these assumptions, the rate of sedimentation can be expressed by the following equation:

$$r = R e^{-k_a D}, \qquad (2)$$

where r (m/m.y.) is rate of sedimentation at given point at a distance D (km) from the trench axis, R (m/m.y.) is a rate of sedimentation at the trench axis, and k_a is a constant.

Assuming the convergence rate of the Cocos and North American plates to be 69 km/m.y. (Minster and Jordan, 1978), the distance of the Site 487 from the trench axis can be calculated by the following equation:

$$D = D_p + 69 \times t, \qquad (3)$$

where D (km) is a distance from the trench axis at t Ma, and D_p (km) is present distance of the site from the trench axis. Using Equations (2) and (3), we can obtain an equation for changing rate of sedimentation with time:

$$r = R e^{-k_a(D_p + 69 t)}. \qquad (4)$$

Table 7. Paleomagnetic results at Site 487, outer rise.

Hole	Core	Section	Interval (cm)	Sub-bottom Depth (m)	AF Demag. Field (Oe)	Relative Declination	Inclination	Intensity ($\times 10^{-6}$ emu/cc)
487	3	4	52.0–54.0	15.53	0	59.2	67.4	5.81
	3	4	52.0–54.0	15.53	150	56.9	78.6	3.24
	5	1	132.0–134.0	30.83	0	252.5	31.7	0.87
	5	1	132.0–134.0	30.83	150	248.8	50.8	0.75
	5	2	65.0–67.0	31.66	0	86.3	−29.1	1.75
	5	2	65.0–67.0	31.66	150	84.5	−37.0	1.54
	5	3	90.0–92.0	33.41	0	90.9	66.9	4.35
	5	3	90.0–92.0	33.41	150	76.6	60.2	3.72
	6	1	60.0–62.0	39.61	150	336.6	46.5	12.73
	6	2	60.0–62.0	41.11	150	244.3	24.0	16.99
	6	3	99.0–101.0	43.00	150	141.4	62.3	13.36
	7	1	25.0–27.0	48.76	150	217.0	27.9	13.07
	7	1	135.0–137.0	49.86	150	338.5	74.2	6.90
	8	1	100.0–102.0	59.01	150	150.6	62.5	13.32
	8	2	135.0–137.0	60.86	150	15.9	45.7	9.23
	8	3	46.0–48.0	61.47	150	158.3	7.5	11.70
	8	4	125.0–127.0	63.76	150	245.8	7.2	6.28
	8	5	88.0–90.0	64.89	150	215.4	41.5	10.76
	8	6	84.0–86.0	66.35	150	262.1	51.0	12.98
	9	1	30.0–32.0	67.81	150	128.4	67.5	10.82
	9	2	135.0–137.0	70.36	150	241.2	64.7	20.63
	9	3	53.0–55.0	71.04	150	170.0	64.9	11.36
	9	4	32.0–34.0	72.33	150	4.0	38.4	9.83
	9	5	118.0–120.0	74.69	150	292.0	73.6	9.72
	9	6	82.0–84.0	75.83	150	59.7	67.2	0.95
	10	7	9.0–11.0	86.10	150	158.1	48.5	0.38
	11	2	98.0–100.0	88.99	150	25.1	−4.7	12.56
	11	4	81.0–83.0	91.82	150	134.9	78.0	4.59
	12	3	76.0–78.0	99.77	150	175.0	−5.1	6.01
	12	4	31.0–33.0	100.82	150	329.7	−13.9	1.89
	12	4	92.0–94.0	101.43	150	210.9	−34.1	9.24
	12	5	41.0–43.0	102.42	150	325.3	49.0	7.48
	13	2	65.0–67.0	107.66	150	2.4	76.4	8.77
	13	3	80.0–82.0	109.31	150	192.6	−38.1	4.10
	13	4	90.0–92.0	110.91	150	115.6	−10.7	12.24
	13	5	33.0–35.0	111.84	150	10.3	19.7	9.59
	14	1	61.0–63.0	115.62	150	251.4	−16.9	4.81
	14	2	100.0–102.0	117.51	0	116.4	35.3	5.39
	14	2	100.0–102.0	117.51	150	166.3	−26.5	0.73
	14	3	42.0–44.0	118.43	150	200.6	−14.3	2.83
	15	2	74.0–76.0	126.75	150	51.4	8.8	3.19
	15	3	67.0–69.0	128.18	150	48.7	−18.8	0.73
	15	4	57.0–59.0	129.58	150	33.2	−3.0	2.62
	15	5	46.0–48.0	130.97	150	211.1	51.0	3.81
	15	6	41.0–43.0	132.42	150	219.5	11.4	1.63
	15	7	26.0–28.0	133.77	150	301.2	3.5	6.75
	16	1	47.0–49.0	134.48	150	33.9	−57.8	8.81
	16	2	66.0–68.0	136.17	150	201.5	−37.6	6.14
	17	2	30.0–32.0	145.31	150	5.5	36.9	1.14
	18	1	68.0–70.0	153.69	150	256.3	39.8	2.48
	18	2	131.0–133.0	155.82	150	71.2	−16.9	5.30
	18	3	73.0–75.0	156.74	150	286.6	50.1	2.42
	18	4	69.0–71.0	158.20	150	204.6	4.0	2.31
	18	5	20.0–22.0	159.21	150	260.0	−15.2	1.52
	18	6	128.0–130.0	161.79	150	63.4	63.6	0.95
	19	2	16.0–18.0	164.17	0	132.2	−0.1	2.83
	19	2	16.0–18.0	164.17	150	181.2	−32.3	2.94

Integrating Equation (4) obtains the thickness of sediments that have accumulated at a given site during a time interval from T_1 to T_2 as follows:

$$H = \int_{T_1}^{T_2} r\, dt = \int_{T_1}^{T_2} R e^{-k_a(D_p + 69\, t)} dt \quad (5)$$

and

$$H = \frac{R}{69\, k_a\, e^{k_a\, D_p}} \left[-e^{-69\, k_a t} \right]_{T_1}^{T_2} . \quad (6)$$

By using magnetostratigraphic data from Site 487, which include the Brunhes/Matuyama boundary of 0.69 Ma at 87.5 meters subdepth and the upper limit of the Jaramillo Event of 0.89 Ma at 90 meters subdepth, we obtain the value of k_a: 0.065. This means the rate of sedimentation decreases one order of magnitude for every 35 km.

If we assume a conformable relationship between rates of sedimentation and the distance from the trench on both the ocean and land sides, a maximum rate and position of sediment accumulation is predicted by the equations. The maximum rate occurs 2 km landward of the topographic trench axis (Fig. 19). Using this maximum rate (900 m/m.y.), we can write the sediment accumulation rate equation at a site with a distance D km from the maximum rate position, as follows (ocean side):

$$r_o = 900e^{-0.065D} \quad (7)$$

and (land side)

$$r_s = 900e^{-0.21D}. \quad (8)$$

Figure 19 shows the relation between the submarine topography and calculated rates of sediment accumulation. In this figure it is noteworthy that the constant-rate line of 10 m/m.y. passes over the sub-bottom depression formed by the Middle America Trench. The constant-rate line connects the outer limit of the gentle upper slope and the inner limit of the flat outer rise at a water depth of 3450 to 3500 meters. This distribution of constant-rate lines means that the sands and fine sediments from turbidity currents are accumulating within

Table 8. Paleomagnetic results and bedding orientations at Site 488, lower slope.

Hole	Core	Section	Interval (cm)	Sub-bottom Depth (m)	AF Demag. Field (Oe)	Relative Declination	Inclination	Intensity ($\times 10^{-6}$ emu/cc)	Bedding Orientation Strike	Dip
488	2	1	103.0–105.5	2.04	150	126.8	5.5	111.41		
	2	1	106.0–108.0	2.07	150	88.1	31.9	10.40		
	2	1	109.0–111.0	2.10	150	294.0	−18.6	43.95		
	2	1	112.0–114.5	2.13	150	91.4	37.8	11.70		
	2	1	114.5–117.5	2.16	150	87.6	38.7	13.52		
	2	4	131.0–133.0	6.82	150	149.3	55.1	6.75		
	3	1	106.0–108.0	11.57	150	224.1	20.4	6.79		
	4	3	10.0–12.5	23.11	150	169.6	26.2	24.50		
	4	3	13.0–15.0	23.14	150	225.0	−31.6	84.97		
	4	3	15.0–17.0	23.16	150	322.7	−10.6	50.34		
	4	3	51.0–53.0	23.52	150	195.2	9.3	6.16		
	4	6	74.0–76.0	28.25	150	122.4	28.7	1.61		
	5	6	60.0–62.0	37.61	150	289.6	30.6	1.07		
	5	6	68.0–70.0	37.69	150	207.3	−31.8	0.74		
	5	6	77.0–79.0	37.78	150	219.6	−12.6	1.13		
	6	6	27.0–29.0	46.78	150	251.9	16.0	15.37		
	9	1	93.0–96.0	68.45	150	284.3	42.9	3.15		
	9	3	27.0–29.0	70.78	150	309.3	60.2	3.83		
	10	4	93.0–95.0	82.44	150	132.9	59.0	5.95		
	11	6	57.0–59.0	94.58	150	280.6	30.4	9.12		
	13	1	45.0–47.0	105.96	150	123.6	27.7	13.51		
	13	3	135.0–137.0	109.86	150	352.1	85.6	0.51		
	13	4	68.0–70.0	110.69	150	68.2	19.1	1.36		
	14	1	130.0–132.0	116.31	150	46.2	37.5	3.37		
	15	2	20.0–22.0	126.21	150	138.1	35.9	5.37		
	16	1	102.0–104.0	135.03	150	318.0	48.9	5.49		
	16	5	6.0–8.0	140.07	150	204.8	24.0	2.79		
	18	1	59.0–61.0	153.60	150	74.6	44.3	13.11		
	18	5	69.0–71.0	159.70	150	153.8	38.6	10.95		
	19	1	13.0–15.0	162.64	150	97.0	29.3	4.54		
	19	5	21.0–23.0	168.72	150	204.8	26.4	24.12		
	20	1	41.0–43.0	172.42	150	124.2	28.3	12.11		
	20	3	131.0–133.0	176.32	150	76.6	50.4	12.16		
	21	1	129.0–131.0	182.80	150	16.3	31.1	19.16		
	21	5	128.0–130.0	188.79	150	79.3	15.2	4.77		
	22	1	112.0–114.0	192.13	150	12.8	31.1	25.27		
	22	3	129.0–131.0	195.30	150	191.8	23.2	1.00		
	23	1	137.0–139.0	201.88	150	240.4	16.9	4.36		
	24	1	66.0–68.0	210.67	150	298.7	28.0	1.14		
	25	1	118.0–120.0	220.69	150	22.6	16.8	8.95		
	26	1	134.0–136.0	230.35	150	259.3	30.8	31.29		
	26	5	78.0–80.0	235.79	150	332.3	58.8	41.02		
	27	1	135.0–137.0	239.86	150	267.7	33.6	17.87		
	29	1	27.0–29.0	257.78	150	141.9	1.0	0.72		
	29	5	9.0–11.0	263.60	150	164.7	−44.0	0.24		
	30	1	122.0–124.0	265.73	150	112.2	54.9	1.43		
	30	5	135.0–137.0	271.86	150	59.7	−9.6	0.05		
	31	1	98.0–100.0	276.99	150	177.0	−68.0	0.82		
	31	3	131.0–132.0	280.32	150	227.2	−46.4	1.14		
	32	1	134.0–136.0	286.35	150	345.1	−53.1	5.18		
	32	3	99.0–101.0	289.00	150	176.0	−33.5	1.59		
	32	4	2.0–4.0	289.53	150	31.8	6.0	1.68		
	32	4	4.0–6.0	289.55	150	267.0	3.0	1.68		
	32	4	7.0–9.0	289.58	150	215.4	−4.7	2.31		
	32	4	10.0–12.0	289.61	150	261.5	−14.0	1.72		
	32	4	13.0–15.0	289.64	150	135.9	−39.7	1.69		
	32	4	16.0–18.0	289.67	150	2.5	−10.3	1.19		
	32	4	30.0–32.0	289.81	150	112.2	12.5	1.54		
	32	4	49.0–51.0	290.00	150	34.6	4.1	1.82		
	32	4	63.0–65.0	290.14	150	320.1	4.6	1.51		
	32	4	87.0–89.0	290.38	150	185.0	1.4	1.89		
	33	1	80.0–82.0	294.81	150	29.8	−0.8	5.53		
	33	5	24.0–26.0	300.25	150	265.8	−6.9	47.50		
	34	1	55.0–57.0	303.56	150	314.5	1.7	8.73		
	34	5	45.0–47.0	309.46	150	283.1	−26.3	9.35		
	37	2	23.0–25.0	335.24	150	342.3	26.2	18.96		
	40	2	1.0–3.0	363.52	150	95.2	20.2	36.62		
	40	2	21.0–23.0	363.72	150	166.7	33.5	15.96		
	42	2	15.0–17.0	382.66	150	207.3	16.0	14.65	N 27W	20E
	42	2	54.0–56.0	383.05	150	200.0	14.5	47.44	20W	20E
	43	1	137.0–139.0	391.88	150	20.2	13.4	12.70	20W	35E
	45	7	55.0–57.0	419.06	150	78.3	17.4	37.50		

Table 9. Paleomagnetic results, Site 489, upper slope.

Hole	Core	Section	Interval (cm)	Sub-bottom Depth (m)	AF Demag. Field (Oe)	Relative Declination	Inclination	Intensity ($\times 10^{-6}$ emu/cc)
489	1	2	119.0–121.0	2.70	150	197.9	−46.6	0.270
	1	4	47.0–49.0	4.98	150	5.8	6.5	0.560
	2	1	134.0–136.0	7.35	150	15.0	−0.8	0.100
	2	5	96.0–98.0	12.97	150	22.1	−2.7	0.100
	3	1	114.0–116.0	16.65	150	133.9	17.0	0.140
	3	5	51.0–53.0	22.02	150	204.6	−62.3	0.090
	4	1	73.0–75.0	25.74	150	226.3	−47.8	0.050
489A	4	1	59.0–61.0	56.10	150	42.1	−82.4	0.001
	4	5	95.0–97.0	62.46	150	349.3	27.3	0.020
	5	1	138.0–140.0	66.39	150	212.5	65.6	0.001
	5	5	80.0–82.0	71.81	150	85.1	−37.2	0.035
	6	1	67.0–69.0	75.18	150	216.5	28.6	0.103
	6	3	141.0–143.0	78.92	150	277.2	56.6	0.248
	7	1	131.0–133.0	85.32	150	319.3	36.0	0.036
	7	5	33.0–35.0	90.34	150	354.1	0.3	0.082
	8	1	129.0–131.0	94.80	150	1.7	34.5	0.014
	8	3	136.0–138.0	97.87	150	250.6	51.6	0.067
	9	2	92.0–94.0	105.43	150	36.6	61.4	0.001
	11	4	68.0–70.0	137.19	150	159.8	21.2	0.017
	12	1	3.0–5.0	131.54	150	27.4	−53.3	0.008
	13	1	145.0–147.0	142.46	150	47.1	10.6	0.082
	15	1	119.0–121.0	161.20	150	346.9	51.5	0.086
	16	4	3.0–5.0	169.04	150	350.9	16.8	0.046
	19	1	55.0–57.0	183.56	150	22.5	30.8	0.328
	20	1	142.0–144.0	189.93	150	354.4	9.1	0.069
	21	3	96.0–98.0	201.97	150	313.6	−22.7	0.178
	21	6	117.0–119.0	206.68	150	5.9	28.1	1.556
	21	1	108.0–110.0	208.59	150	208.7	30.5	0.315
	22	5	57.0–59.0	214.08	150	41.2	−39.1	0.533
	23	2	109.0–111.0	219.60	150	154.0	21.7	0.234
	23	5	132.0–134.0	224.33	150	139.5	−54.4	0.177
	24	2	38.0–40.0	228.39	150	24.2	24.5	0.235
	24	6	40.0–42.0	234.41	150	298.0	65.3	0.054
	25	2	139.0–141.0	238.90	150	333.5	−20.0	0.008
	25	5	112.0–114.0	243.13	150	5.0	−6.0	0.011
	26	1	124.0–126.0	246.75	150	55.4	−28.3	0.082
	26	4	58.0–60.0	250.59	150	176.8	−71.3	0.048
	27	3	130.0–132.0	259.31	150	30.6	−55.2	0.105
	28	2	100.0–102.0	266.51	150	88.6	27.5	0.059
	29	1	138.0–140.0	274.39	150	57.1	−4.7	0.130
	29	5	102.0–104.0	280.03	150	33.6	−28.0	0.128
	30	2	82.0–84.0	284.33	150	38.1	27.3	0.270
	30	5	105.0–107.0	289.06	150	250.9	−77.4	0.196
	31	2	80.0–82.0	293.31	150	199.6	−27.2	0.071

the topographic depression along the Middle America Trench.

The total accumulation rate along the Middle America Trench can be calculated using Equations (7) and (8). The total volume of the sediments accumulated in the trench is represented by the area of the sediments in cross section, which can be calculated by integrating Equations (7) and (8).

$$S = \int_0^\infty r_o \, dD + \int_0^\infty r_s \, dD = \int_0^\infty 0.9 e^{-0.065D} \, dD$$

$$+ \int_0^\infty 0.9 e^{-0.21D} \, dD$$

$$S = \left[-\frac{0.9 e^{-0.065D}}{0.065} \right]_0^\infty + \left[-\frac{0.9 e^{-0.21D}}{0.21} \right]_0^\infty$$

$$S = \frac{0.9}{0.065} + \frac{0.9}{0.21} = 13.8 + 4.3 = 18.1,$$

where S is the area of sediments accumulated during 1 m.y. in km² (on the cross section).

The porosity of accumulating sediments during last 0.69 m.y. (Shephard et al., this volume) are listed in the following table.

Site	Porosity of Volume Base (%)	Porosity of Area Base (%)	Thickness (m)
492	66	51	9.5
491	61	48	22.0
488	decrease from 65 to 45 with subdepth	49–33	258.0
487	78	64	87.5

The weighted average porosity is 47% for the accumulating sediments. Thus the total amount of accumulating sediments along the trench area without pore space is 9.6 km²/m.y. (18.1 × 0.53). As the area of sediment accretion under the lower slope is 106.9 km² and the estimated porosity of area base is 23% (33% of volume base), the sediment under the lower slope can be accreted for 8.6 m.y., assuming accretion from the accumulation of sediment along the trench area. The calculated duration is consistent with the oldest age of cored sediments in the upper part of the lower slope at Site 492.

Magnetization Boundary in Lower Slope and Outer Rise

There is a noticeable variety in intensity of remanent magnetization of the sediments accumulated in the lower slope and outer rise areas during last 0.69 m.y.:

Table 10. Paleomagnetic results and bedding orientation at Site 490, upper slope.

Hole	Core	Section	Interval (cm)	Sub-bottom Depth (m)	AF Demag. Field (Oe)	Relative Declination	Inclination	Intensity (×10⁻⁶ emu/cc)	Bedding Orientation Strike	Dip
490	1	1	100.0–102.0	1.01	150	344.2	−35.9	0.115		
	1	2	120.0–122.0	2.71	150	129.0	10.0	0.382		
	1	3	35.0–37.0	3.36	150	173.4	−12.9	0.140		
	1	4	95.0–97.0	5.46	150	320.8	−33.4	0.194		
	2	1	85.0–87.0	7.86	150	145.3	11.7	0.291		
	2	6	87.0–89.0	15.38	150	240.5	28.6	0.149		
	3	2	131.0–133.0	18.32	150	114.3	−5.9	0.001		
	3	5	100.0–102.0	22.51	150	336.1	−9.7	0.019		
	4	2	129.0–131.0	27.80	150	350.3	53.7	0.037		
	4	5	40.0–42.0	31.41	150	265.2	33.7	0.013		
	5	1	128.0–130.0	35.79	150	291.6	−28.5	0.005		
	5	6	95.0–97.0	42.96	150	264.2	40.6	0.006		
	6	2	104.0–106.0	46.55	150	12.7	53.5	0.167		
	6	5	52.0–54.0	50.53	150	157.2	−3.4	0.074		
	7	1	141.0–143.0	54.92	150	335.6	68.5	0.580		
	7	3	112.0–114.0	57.63	150	301.4	−16.2	0.581		
	8	1	144.0–146.0	64.45	150	90.0	2.8	0.001		
	8	4	112.0–114.0	68.63	150	257.9	60.8	0.001		
	9	2	144.0–146.0	75.45	150	13.0	−34.9	1.470		
	10	1	138.0–140.0	83.39	150	112.2	−44.0	0.993		
	10	5	43.0–45.0	88.44	150	166.6	5.8	0.990		
	11	1	97.0–99.0	92.48	150	357.1	−20.9	0.025		
	12	2	144.0–146.0	106.95	150	211.8	−12.3	0.052		
	15	1	130.0–132.0	133.81	150	73.2	12.3	0.414		
	15	5	36.0–38.0	138.87	150	28.5	−28.3	6.869		
	16	1	139.0–141.0	143.40	150	252.0	−50.7	1.033		
	16	4	43.0–45.0	146.94	150	81.4	−29.1	3.409		
	17	3	144.0–146.0	155.95	150	10.4	5.1	14.266		
	17	5	61.0–63.0	158.12	150	52.5	10.0	0.488		
	18	1	143.0–145.0	162.44	150	64.6	45.5	0.130		
	18	5	100.0–102.0	168.01	150	258.6	−24.7	1.817		
	20	1	144.0–146.0	181.45	150	12.2	−17.5	9.684		
	20	5	129.0–131.0	187.30	150	152.6	−31.8	1.215		
	21	1	140.0–142.0	190.91	150	22.3	−20.3	7.969		
	21	5	100.0–102.0	196.51	150	185.0	19.1	27.463		
	22	1	143.0–145.0	200.44	150	54.6	−22.1	10.307		
	22	5	139.0–141.0	206.40	150	281.0	−29.0	0.995		
	23	1	144.0–146.0	209.95	150	21.4	−11.6	0.384		
	23	5	98.0–100.0	215.49	150	126.5	−56.3	0.037		
	24	1	124.0–126.0	219.25	150	358.7	28.5	0.144		
	24	5	44.0–46.0	224.45	150	332.9	−16.4	0.582		
	25	2	144.0–146.0	230.45	150	4.1	−18.1	0.009		
	26	2	145.0–147.0	239.96	150	135.5	−27.5	5.570		
	26	6	128.0–130.0	245.79	150	104.7	−34.3	3.834		
	27	1	144.0–146.0	247.95	150	37.8	65.5	0.277		
	27	3	146.0–148.0	250.97	150	48.8	43.9	0.561		
	28	1	136.0–138.0	257.37	150	67.8	46.1	1.112		
	28	5	142.0–146.0	263.44	150	112.8	29.1	1.678		
	29	1	92.0–94.0	266.43	150	119.6	32.1	0.002		
	29	4	119.0–121.0	271.20	150	234.4	41.2	0.003		
	29	7	64.0–66.0	275.15	150	65.2	15.9	0.039		
	30	3	7.0–9.0	278.08	150	278.8	−5.7	0.006		
	31	2	29.0–31.0	286.30	150	217.0	28.6	0.029		
	33	1	86.0–88.0	299.87	150	283.3	48.6	0.008		
490	34	1	135.0–137.0	304.86	150	329.4	−9.4	0.681		
	34	4	29.0–31.0	308.30	150	355.6	51.9	0.404		
	35	2	75.0–77.0	315.26	150	290.4	−16.8	0.204		
	35	5	100.0–102.0	320.01	150	277.0	7.2	0.252		
	36	1	143.0–145.0	323.94	150	170.1	−57.8	0.633		
	36	5	143.0–145.0	329.94	150	338.9	18.2	0.177		
	37	1	144.0–146.0	333.45	150	199.7	45.8	0.753		
	37	5	143.0–145.0	339.44	150	232.7	43.8	0.892		
	38	2	142.0–144.0	344.43	150	156.4	26.6	0.939		
	38	5	142.0–144.0	348.93	150	107.3	38.5	0.706	N 73E	20N
	39	2	137.0–139.0	353.88	150	336.0	25.9	1.835	24E	10W
	39	5	112.0–114.0	358.13	150	182.6	40.3	0.321		
	40	2	75.0–77.0	362.76	150	50.9	−18.2	0.738	N 51W	40W
	40	6	101.0–103.0	369.02	150	136.2	−3.7	1.742	44E	30W
	41	1	98.0–100.0	370.99	150	15.7	−20.2	0.425	16W	30W
	42	2	29.0–31.0	381.30	150	356.1	−3.6	0.789	4E	40W
	42	5	6.0–8.0	385.57	150	45.7	−28.6	0.406	46W	50W
	43	1	128.0–130.0	390.29	150	137.6	−3.8	0.329	42E	75W
	43	3	100.0–102.0	393.01	150	126.8	26.4	0.396	53E	60W
	44	2	122.0–124.0	401.23	150	328.8	15.0	0.160	31E	63W
	44	2	126.0–128.0	401.27	150	330.1	11.2	0.760	30E	63W
	47	1	64.0–66.0	423.15	150	130.7	23.4	0.113	1W	81W
	48	1	82.0–84.0	427.83	150	134.9	11.2	0.215	6E	52W
	49	1	123.0–125.0	437.74	150	124.8	8.6	0.049	NS	60W
	50	1	91.0–93.0	446.92	150	326.6	70.8	0.045	N 33E	45W
	51	1	97.0–99.0	456.48	150	9.9	−17.4	0.009	10W	33W
	53	1	104.0–106.0	475.55	150	353.7	−28.6	0.064	6E	50W
	54	1	82.0–84.0	484.83	150	177.3	−11.1	0.023	3E	35W
	54	4	87.0–89.0	489.38	150	327.4	−19.5	0.281	33E	30W
	55	1	58.0–60.0	494.09	150	341.0	−18.0	0.232	19E	30W
	55	3	103.0–105.0	497.54	150	274.4	−4.8	0.146	86E	30N
	56	1	67.0–69.0	503.68	150	25.3	14.2	0.168	25W	40W
	56	5	88.0–90.0	509.89	150	277.0	25.2	0.918	20E	46W
	57	2	21.0–23.0	514.22	150	119.5	21.4	0.821	6E	45W
	57	5	96.0–98.0	519.47	150	340.0	48.9	0.324	12W	40W
	58	1	19.0–21.0	522.20	150	355.0	27.2	0.427	5E	35W
	58	5	60.0–62.0	528.61	150	326.6	19.9	0.877	13E	30W
	59	1	80.0–82.0	532.31	150	206.5	25.8	0.674	2W	38W
	59	3	40.0–42.0	534.91	150	342.5	14.7	2.145	17E	35W
	59	4	6.0–8.0	536.07	150	332.3	30.3	0.534	4E	38W
	59	4	11.0–13.0	536.12	150	318.7	21.5	0.404	17E	38W
	60	1	73.0–75.0	541.74	150	173.0	18.2	0.411	7E	28W
	60	4	3.0–5.0	545.54	150	142.1	36.4	0.349	38E	35W
	61	1	78.0–80.0	551.29	150	307.2	23.5	0.188	29E	25W
	61	3	129.0–131.0	554.80	150	105.0	−4.7	0.053	75E	27N
	61	3	134.0–136.0	554.85	150	72.7	58.3	0.052	73W	27N
	62	1	66.0–68.0	560.67	150	80.9	−8.1	0.119	81W	25N
	62	4	62.0–64.0	565.13	150	141.0	6.2	0.220	38E	30W
	63	2	23.0–25.0	571.24	150	99.4	25.7	0.163	81E	25N
	64	1	146.0–148.0	580.47	150	334.1	14.6	0.584	24E	32W

Table 11. Paleomagnetic results and bedding orientation at Site 491, lower slope.

Hole	Core	Section	Interval (cm)	Sub-bottom Depth (m)	AF Demag. Field (Oe)	Relative Declination	Inclination	Intensity ($\times 10^{-6}$ emu/cc)	Bedding Orientation Strike	Dip	Remarks
491	1	2	140.0–142.0	2.91	150	308.2	11.0	0.262			
	1	5	82.0–84.0	6.83	150	62.7	49.3	0.317			
	2	1	140.0–142.0	11.41	150	153.4	4.2	20.529			
	2	4	113.0–115.0	15.64	150	142.2	15.8	0.284			
	3	1	144.0–146.0	20.95	150	115.6	6.3	0.145			
	3	5	129.0–131.0	26.80	150	2.2	−31.0	0.103			
	4	2	115.0–117.0	31.66	150	163.1	31.6	0.146			
	4	5	106.0–108.0	36.07	150	200.6	64.6	0.098			
	5	4	42.0–44.0	43.43	150	311.7	27.2	0.036			
	6	2	38.0–40.0	49.89	150	123.9	−16.8	0.235			
	6	5	136.0–138.0	55.37	150	80.4	12.8	0.377			
	7	1	137.0–139.0	58.88	150	272.8	18.3	0.066			
	7	5	113.0–115.0	64.64	150	46.8	33.0	0.074			
	8	1	137.0–139.0	68.38	150	93.1	−46.0	0.086			
	8	5	113.0–115.0	74.14	150	39.4	47.8	0.778			
	9	1	133.0–135.0	77.84	150	254.4	−18.7	8.363			
	9	5	134.0–136.0	83.85	150	358.0	51.0	3.708			
	10	2	66.0–68.0	88.17	150	2.4	−11.8	5.124			
	10	5	127.0–129.0	93.28	150	87.6	58.1	7.587			
	11	1	126.0–128.0	96.77	150	18.1	−25.6	4.414			
	11	3	115.0–117.0	99.66	150	355.7	15.2	6.471			
	13	2	25.0–27.0	106.76	150	37.2	63.0	3.504	N 53E	24N	
	14	1	133.0–135.0	115.84	150	306.1	−4.4	0.547	54E	24N	
	14	5	56.0–58.0	121.07	150	43.2	13.9	3.267	43W	24W	"A"
	15	2	105.0–107.0	126.56	150	158.3	−61.6	0.148	22E	26W	"A"
	15	3	64.0–66.0	127.65	150	95.5	−2.9	0.805	84E	32W	
	15	5	20.0–22.0	130.21	150	79.2	36.7	0.577	79W	27S	"A"
	16	4	57.0–59.0	138.58	150	65.1	−14.0	0.618	65W	30N	
	16	6	15.0–17.0	141.16	150	257.0	−27.5	2.364	82E	30N	
	17	2	60.0–62.0	145.11	150	103.5	8.2	6.039	76E	43N	
	17	4	50.0–52.0	148.01	150	83.7	1.7	3.140	84W	30N	
	18	4	25.0–27.0	157.26	150	342.2	−62.0	0.195	85W	21N	
	19	3	56.0–58.0	165.57	150	116.1	3.8	3.203	40W	28W	"B"
	20	2	121.0–123.0	174.22	150	78.9	29.4	3.415			
	21	3	90.0–92.0	184.91	150	297.4	−13.9	4.188			
	25	1	85.0–87.0	210.36	150	291.4	45.4	0.809	N 64E	62N	
	25	3	73.0–75.0	213.24	150	289.1	33.0	4.743	73E	63N	
	26	5	14.0–16.0	225.15	150	92.2	60.6	0.061	88E	58N	
	27	5	96.0–98.0	235.47	150	108.7	27.8	7.249	63E	63N	
	30	5	20.0–22.0	263.21	150	183.3	−38.0	2.050	3W	43W	"C"
	31	5	22.0–24.0	272.73	150	59.7	7.4	1.948	89W	30N	
	32	5	28.0–30.0	282.29	150	168.3	−5.7	6.975	19W	25W	"C"
	33	2	145.0–147.0	288.46	150	97.4	−1.0	8.554	87E	25N	
	36	5	136.0–138.0	321.37	150	292.4	−7.5	4.253	52E	15N	
	37	4	34.0–36.0	328.35	150	92.7	15.6	5.939	87E	30N	
	39	3	4.0–6.0	345.55	150	28.2	21.0	1.103	10E	45E	"D"
	41	2	126.0–128.0	364.27	150	38.1	−7.4	0.806	38W	31N	
	41	3	114.0–116.0	365.65	150	236.8	−24.7	0.290	33W	39N	
	43	2	134.0–136.0	383.35	150	69.6	−4.2	0.931	65W	26N	
	43	5	88.0–90.0	387.39	150	8.4	−9.4	4.793	15W	35E	
	44	3	27.0–29.0	393.28	150	193.1	−15.3	2.811	13W	28E	
	45	2	144.0–146.0	402.45	150	357.5	−41.6	0.906	3E	24W	"D"
	46	1	110.0–112.0	410.11	150	172.6	1.0	4.007	40E	28W	
	47	3	11.0–13.0	421.62	150	290.6	−38.0	5.102	33E	41E	"D"
	48	6	134.0–136.0	436.85	150	227.4	−1.0	1.649	82E	20N	
	49	3	60.0–62.0	441.11	150	68.2	−9.1	4.896	68W	20N	
	50	2	18.0–20.0	448.69	150	231.9	−10.1	9.709	88W	21N	
	50	2	132.0–134.0	449.83	150	224.1	−19.7	10.911	75E	10N	
	54	1	50.0–52.0	485.51	150	247.2	−27.4	4.051	22W	4E	
	55	2	15.0–17.0	496.16	150	188.8	−15.6	17.902	69E	14N	
	55	3	54.0–56.0	498.05	150	358.2	−17.1	3.190	69E	8N	
	56	1	73.0–75.0	504.74	150	279.2	−25.9	7.433	51E	8N	
	57	3	30.0–32.0	516.81	150	140.8	−5.2	8.194	55W	28N	
	57	3	145.0–147.0	517.96	150	6.6	−12.4	15.327	10W	16E	
	58	1	12.0–14.0	523.13	150	13.1	−10.7	10.251	3W	19E	
	58	1	88.0–90.0	523.89	150	257.3	5.7	4.453	42W	16E	
	59	1	56.0–58.0	533.07	150	316.2	−53.3	0.594	54E	6E	

Table 12. Paleomagnetic results and bedding orientation, Site 492, lower slope.

Hole	Core	Section	Interval (cm)	Sub-bottom Depth (m)	AF Demag. Field (Oe)	Relative Declination	Inclination	Intensity ($\times 10^{-6}$ emu/cc)	Bedding Orientation Strike	Dip	Remarks
492	1	1	80.0–82.0	0.81	150	42.7	15.7	0.250			
	1	1	130.0–132.0	1.31	150	215.1	−39.8	43.926			
	1	2	64.0–66.0	2.15	150	228.1	19.4	0.155			
	1	3	21.0–23.0	3.22	150	22.0	59.2	0.084			
	2	1	90.0–92.0	4.41	150	158.3	−22.1	1.425			
	2	2	141.0–143.0	6.42	150	270.3	57.3	0.764			
	2	3	138.0–140.0	7.89	150	139.3	59.1	0.264			
	2	4	94.0–96.0	8.95	150	115.1	16.6	0.367			
	3	1	17.0–19.0	13.18	150	265.7	−27.2	0.222			
	3	2	65.0–67.0	15.16	150	273.6	71.6	0.034			
	3	4	34.0–36.0	17.85	150	4.4	41.4	0.064			
	3	5	39.0–41.0	19.40	150	122.4	−38.8	0.088			
	4	1	117.0–119.0	23.68	150	212.0	10.6	0.007			
	4	6	31.0–33.0	30.32	150	125.2	−2.7	0.013			
	4	7	15.0–17.0	31.66	150	106.2	−3.1	0.015			
	5	1	109.0–111.0	33.10	150	355.4	16.0	0.152			
	5	2	102.0–104.0	34.53	150	61.2	−20.1	0.151			
	5	3	100.0–102.0	36.01	150	69.1	20.4	0.177			
	5	4	84.0–86.0	37.35	150	183.1	41.2	0.183			
	6	1	118.0–120.0	42.69	150	28.3	70.2	0.181			
	6	2	120.0–122.0	44.21	150	325.0	−1.3	0.347			
	6	3	120.0–122.0	45.71	150	283.1	67.2	0.148			
	6	4	116.0–118.0	47.17	150	125.0	29.9	0.229			
	6	5	100.0–102.0	48.51	150	205.3	−16.4	0.149			
	7	3	44.0–46.0	54.45	150	3.7	18.9	0.165			
	8	1	138.0–140.0	61.89	150	301.2	56.4	0.013			
	8	3	107.0–109.0	64.58	150	236.3	36.8	0.021			
	9	1	127.0–129.0	71.28	150	192.9	44.7	15.308			
	9	2	127.0–129.0	72.78	150	248.7	36.2	0.109			
	10	2	110.0–112.0	82.11	150	312.2	15.9	0.039			
	11	1	47.0–49.0	89.48	150	317.4	28.8	0.185			
	11	2	78.0–80.0	91.29	150	332.9	31.6	0.052			
	12	5	123.0–125.0	105.74	150	230.2	25.9	0.110			
	13	2	142.0–144.0	110.93	150	353.7	31.3	0.518	N 6E	29W	
	14	3	21.0–23.0	120.72	150	103.8	40.7	0.151			
	14	3	25.0–27.0	120.76	150	143.7	−24.6	0.183	N 36E	45W	
	14	3	45.0–47.0	120.96	150	365.2	15.2	0.263	4E	31W	
	18	4	27.0–29.0	160.28	150	67.9	2.0	0.108	89W	14S	
	19	3	69.0–71.0	168.70	150	115.9	24.4	1.240	64E	34S	
	20	6	24.0–26.0	182.25	150	301.4	34.3	0.071	59E	44N	
	20	6	85.0–87.0	182.86	150	128.6	−27.7	0.133	NS	39E	"E"
	24	2	16.0–18.0	214.17	150	28.8	−53.3	0.286	81W	74S	
	25	1	100.0–102.0	223.01	150	14.9	1.1	0.549	83W	43S	
	25	5	101.0–103.0	229.02	150	187.3	25.1	1.529	7W	42E	
	26	2	90.0–92.0	233.91	150	157.8	−38.3	5.552	22E	35W	
	26	2	131.0–133.0	234.32	150	128.0	−26.5	8.940	42E	29W	
	27	5	112.0–114.0	248.13	150	355.1	46.5	0.288	5E	38W	
492A	1	1	20.0–22.0	0.21	150	45.9	51.7	0.104			
	1	1	69.0–71.0	0.70	150	313.9	30.7	0.608			
	1	1	130.0–132.0	1.31	150	313.5	31.4	0.867			
	1	2	11.0–13.0	1.62	150	142.7	28.4	1.065			
	1	2	90.0–92.0	2.41	150	153.6	32.2	0.561			
	1	3	12.0–14.0	3.13	150	298.5	32.2	0.292			
	1	3	77.0–79.0	3.78	150	320.2	65.8	0.789			
	2	1	106.0–108.0	5.32	150	116.0	39.2	1.910			
	2	2	30.0–32.0	6.06	150	143.9	−58.4	0.654			
	2	2	97.0–99.0	6.73	150	154.0	−47.0	1.336			
	2	3	57.0–59.0	7.83	150	355.7	25.1	0.592			
	3	1	45.0–47.0	14.21	150	121.6	38.0	0.243			
	3	1	114.0–116.0	14.90	150	90.4	37.2	0.378			
	3	2	27.0–29.0	15.53	150	336.4	36.6	0.423			
	4	1	75.0–77.0	19.26	150	313.5	53.5	0.286			
	4	2	9.0–11.0	20.10	150	264.9	−28.1	0.163			
	4	2	71.0–73.0	20.72	150	291.0	35.1	0.302			
	5	1	56.0–58.0	23.82	150	314.0	10.9	0.264			
	5	1	124.0–126.0	24.50	150	141.7	20.7	0.105			
	5	2	46.0–48.0	25.22	150	320.4	28.2	0.270			
	6	1	68.0–70.0	28.69	150	9.3	31.3	0.275			
	6	1	144.0–146.0	29.45	150	59.1	45.6	0.167			
	6	2	44.0–46.0	29.95	150	92.4	34.5	0.231			
	6	2	131.0–133.0	30.82	150	42.2	29.0	0.251			
	7	1	51.0–53.0	33.27	150	148.6	39.0	0.154			
	7	1	117.0–119.0	33.93	150	273.9	26.2	0.065			
	7	2	51.0–53.0	34.77	150	42.4	60.9	0.156			
	8	1	30.0–32.0	37.81	150	32.4	−18.6	0.161			
	8	1	112.0–114.0	38.63	150	78.6	18.5	0.164			
	9	1	72.0–74.0	42.98	150	58.3	51.3	0.294			
	10	1	18.0–20.0	47.19	150	154.9	75.5	0.323			

Table 13. Paleomagnetic results and bedding orientation, Site 493, upper slope.

Hole	Core	Section	Interval (cm)	Sub-bottom Depth (m)	AF Demag. Field (Oe)	Relative Declination	Inclination	Intensity ($\times 10^{-6}$ emu/cc)	Bedding Orientation Strike	Dip	Remarks
493	1	1	91.0–93.0	0.92	150	45.7	40.1	1.508			
	1	1	91.0–93.0	0.92	−150	44.9	43.8	2.493			
	1	2	91.0–93.0	2.42	150	226.0	26.2	1.755			
	1	2	91.0–93.0	2.42	−150	236.6	24.1	3.098			
	1	3	91.0–93.0	3.92	150	162.5	28.9	1.865			
	1	3	91.0–93.0	3.92	−150	162.4	29.5	3.581			
	1	4	91.0–93.0	5.42	150	231.5	41.5	0.803			
	1	4	91.0–93.0	5.42	−150	241.9	49.7	1.688			
	2	1	131.0–133.0	121.32	150	125.8	14.4	0.053			
	2	1	131.0–133.0	121.32	−150	323.9	25.2	0.064			
	2	3	126.0–128.0	124.27	150	177.7	−53.0	0.085			
	2	3	126.0–128.0	124.27	−150	38.7	−39.2	0.183			
	3	1	120.0–122.0	130.71	150	51.7	22.3	0.228			
	3	1	120.0–122.0	130.71	−150	39.6	60.9	0.078			
	4	2	41.0–43.0	140.92	150	330.7	−20.0	0.308			
	4	2	41.0–43.0	140.92	−150	318.3	−13.2	0.211			
	5	2	30.0–32.0	150.31	150	153.5	−16.5	0.073			
	5	2	30.0–32.0	150.31	−150	80.4	33.6	0.071			
	5	4	30.0–32.0	153.31	150	64.8	15.8	0.093			
	5	4	30.0–32.0	153.31	−150	355.6	24.0	0.091			
	6	2	90.0–92.0	160.41	150	166.4	−33.6	0.024			
	6	2	90.0–92.0	160.41	−150	316.8	−16.1	0.051			
	7	2	90.0–92.0	169.91	150	354.2	−35.1	0.078			
	7	2	90.0–92.0	169.91	−150	314.3	−30.7	0.127			
	8	2	100.0–102.0	179.51	150	216.2	86.1	0.131			
	8	2	100.0–102.0	179.51	−150	312.4	48.6	0.193			
	8	4	100.0–102.0	182.51	150	214.1	2.4	0.368			
	8	4	100.0–102.0	182.51	−150	215.6	−5.2	0.264			
	9	1	80.0–82.0	187.31	150	1.4	20.6	0.145			
	9	1	80.0–82.0	187.31	−150	26.2	12.0	0.147			
	9	3	70.0–72.0	190.21	150	19.6	37.2	0.516			
	9	3	70.0–72.0	190.21	−150	44.9	27.4	0.228			
	10	2	60.0–62.0	198.11	150	295.1	4.4	0.236			
	10	2	60.0–62.0	198.11	−150	321.9	25.3	0.233			
	10	4	60.0–62.0	201.11	150	229.5	−17.9	1.015			
	10	4	60.0–62.0	201.11	−150	231.4	−19.4	0.580			
	11	1	66.0–68.0	206.17	150	298.5	11.0	0.686			
	11	1	66.0–68.0	206.17	−150	304.4	9.4	0.431			
	11	3	66.0–68.0	209.17	150	153.9	28.8	0.057			
	11	3	66.0–68.0	209.17	−150	317.5	30.4	0.170			
	12	1	39.0–41.0	215.40	150	18.0	38.2	0.045			
	12	1	39.0–41.0	215.40	−150	281.7	−56.7	0.035			
	13	1	87.0–89.0	225.38	150	132.7	26.2	0.184			
	13	1	87.0–89.0	225.38	−150	72.3	63.9	0.049			
	14	3	28.0–30.0	237.29	150	255.5	−12.6	0.221			
	14	3	28.0–30.0	237.29	−150	261.7	−35.2	0.323			
	14	5	92.0–94.0	240.93	150	347.2	19.6	0.179			
	15	2	105.0–107.0	246.06	150	332.2	−20.5	0.662			
	15	2	105.0–107.0	246.06	−150	333.5	−38.1	0.325			
	15	4	105.0–107.0	249.06	150	221.2	−15.1	1.488			
	15	4	105.0–107.0	249.06	−150	231.4	−21.0	0.821			
	17	2	5.0–7.0	264.06	150	238.6	−63.3	0.097			
	17	2	5.0–7.0	264.06	−150	21.3	50.0	0.073			
	17	4	3.0–5.0	267.04	150	223.7	−16.2	0.141			
	17	4	3.0–5.0	267.04	−150	266.2	−13.8	0.080			
	18	2	127.0–129.0	274.78	150	147.6	−41.9	0.119			
	18	3	13.0–15.0	275.14	150	153.2	−72.4	0.047			
	18	3	13.0–15.0	275.14	−150	188.0	−14.0	0.097			
	18	5	12.0–14.0	278.13	150	271.2	10.6	0.366	N 1W	13E	"S"
	18	5	12.0–14.0	278.13	−150	274.9	21.1	0.182			
	19	1	44.0–46.0	281.95	150	128.0	−29.6	0.086			
	19	1	44.0–46.0	281.95	−150	317.7	27.0	0.202			
	19	4	66.0–68.0	286.67	150	297.1	−20.2	0.167	N 19E	42W	"S"
493	20	1	63.0–65.0	291.64	150	359.7	16.7	0.263			
	20	5	5.0–7.0	297.06	150	71.2	−5.1	0.389			
	21	2	76.0–78.0	302.77	150	43.4	−33.8	0.088			
	21	2	76.0–78.0	302.77	−150	26.3	7.3	0.046			
	21	4	13.0–15.0	305.14	150	37.9	−71.2	0.177			
	21	4	13.0–15.0	305.14	−150	141.8	1.8	0.048			
	22	2	41.0–43.0	311.92	150	85.6	−23.3	0.275			
	22	4	97.0–99.0	315.48	150	321.2	4.5	0.191			
	24	1	123.0–125.0	330.24	150	165.6	−81.1	0.059			
	24	1	123.0–125.0	330.24	−150	321.9	−31.5	0.065			
	24	5	50.0–52.0	335.51	150	320.3	−3.1	0.242			
	25	2	2.0–4.0	340.03	150	334.1	−0.4	0.290			
	25	6	16.0–18.0	346.17	150	316.5	−27.1	0.167			
	27	1	12.0–14.0	357.63	150	1.9	−0.6	0.222			

Table 13. (Continued).

Hole	Core	Section	Interval (cm)	Sub-bottom Depth (m)	AF Demag. Field (Oe)	Relative Declination	Inclination	Intensity ($\times 10^{-6}$ emu/cc)	Bedding Orientation Strike	Dip	Remarks
493	27	5	2.0–4.0	363.53	150	347.6	60.8	0.210	N 61E	11S	
	28	4	92.0–94.0	372.43	150	192.8	29.4	0.139	77E	27N	] "A
	29	2	41.0–43.0	378.42	150	24.2	68.7	0.150	53E	39N	
	29	5	3.0–5.0	382.54	150	93.9	40.3	0.105	28E	34E	
	30	1	30.0–32.0	386.31	150	272.9	62.7	0.500	69E	17S	
	30	3	141.0–143.0	390.42	150	172.0	51.5	0.543	19W	19E	
	30	5	78.0–80.0	392.79	150	110.4	66.9	0.374	45E	22S	
	31	1	59.0–61.0	396.10	150	337.7	24.4	0.148	45E	22S	
	31	4	120.0–122.0	401.21	150	97.3	36.2	0.157	75W	11S	
	32	1	31.0–33.0	405.32	150	152.4	34.0	0.297	37E	24E	
	32	3	75.0–77.0	408.76	150	68.4	82.9	0.082	73W	22S	
	33	1	140.0–142.0	415.91	150	307.5	55.5	0.124	52E	21S	
	34	1	78.0–80.0	424.79	150	88.6	47.4	0.016			
	34	4	66.0–68.0	429.17	150	249.0	46.0	0.281			
	35	1	56.0–58.0	434.07	150	48.7	31.4	0.331	N 49W	13S	
	35	4	30.0–32.0	438.31	150	197.9	39.7	0.319	14E	10W	] "B"
	36	1	22.0–24.0	443.23	150	137.1	73.0	0.080	22W	8E	
	36	4	129.0–131.0	448.80	150	85.5	14.2	0.279	59W	18N	
	37	1	54.0–56.0	453.05	150	234.5	–53.9	0.008			
	38	1	127.0–129.0	463.28	150	355.1	41.5	0.232	N 5E	24W	"B"
	38	3	66.0–68.0	465.67	150	160.9	20.9	0.037			
	39	1	111.0–113.0	472.62	150	63.9	35.1	0.019			
	39	4	27.0–29.0	476.28	150	71.3	33.8	0.015			
	40	2	54.0–56.0	483.05	150	340.6	53.4	0.005			
	41	1	54.0–56.0	491.05	150	51.0	–4.6	0.275			
	41	3	20.0–22.0	493.71	150	216.6	77.3	0.150			
	42	2	29.0–31.0	501.80	150	146.3	46.5	0.256	N 34E	18W	] "B"
	42	4	87.0–89.0	505.38	150	310.8	23.9	0.135	59E	8W	
	43	1	92.0–94.0	510.43	150	53.9	22.7	0.603	73W	16S	
	43	4	26.0–28.0	514.27	150	266.6	37.2	0.411	87W	13S	
	44	3	66.0–68.0	522.67	150	319.6	12.8	0.586			
	44	5	14.0–16.0	525.15	150	352.2	17.1	0.580			
	45	2	89.0–91.0	530.90	1!	30.6	17.8	0.334	N 84W	19S	
	45	3	136.0–138.0	532.87	150	207.4	34.2	0.472	23E	18E	
	46	1	46.0–48.0	538.47	150	4.9	39.6	0.294	53W	16S	
	46	3	77.0–79.0	541.78	150	299.3	61.4	0.295	74W	11S	
	47	1	48.0–50.0	547.99	150	70.4	34.8	0.404	62E	16S	
	47	3	100.0–102.0	551.51	150	314.5	81.5	0.126	22E	28E	
	48	1	81.0–83.0	557.82	150	99.4	71.4	0.277	43E	33E	
	48	3	24.0–26.0	560.25	150	235.5	79.6	0.147	77W	23S	
	49	1	102.0–104.0	567.53	150	38.8	30.3	0.586	38W	7S	
	49	4	35.0–37.0	571.36	150	196.0	40.8	0.356	88W	24S	
	49	6	119.0–121.0	575.20	150	135.8	32.7	0.189	43W	13S	
	50	2	146.0–148.0	578.97	150	31.7	69.3	0.125	43W	20S	
	50	4	64.0–66.0	581.15	150	64.2	48.7	0.073	87E	26S	
	51	1	98.0–100.0	586.49	150	288.3	3.7	0.021			
	54	3	64.0–66.0	617.65	150	137.5	29.4	0.070	N 10E	31E	
493A	1	2	11.0–13.0	1.62	150	296.1	51.5	2.706			
	2	1	23.0–25.0	2.74	150	306.0	47.7	2.380			
	2	2	31.0–32.0	4.32	150	74.6	45.3	6.073			
	2	3	64.0–66.0	6.15	150	161.5	41.9	1.370			
493B	1	4	30.0–32.0	16.81	150	265.0	32.8	0.537			
	2	1	15.0–17.0	21.66	150	151.9	–5.7	0.775			
	2	2	65.0–67.0	23.66	150	155.9	41.7	0.852			
	2	5	87.0–89.0	28.38	150	211.9	–11.5	0.286			
	3	3	42.0–44.0	34.43	150	181.0	–3.5	0.193			
	3	4	20.0–22.0	35.71	150	145.9	26.7	0.362			
	3	5	58.0–60.0	37.59	150	320.6	18.7	0.451			
	3	6	43.0–45.0	38.94	150	214.8	2.6	0.228			
	4	6	144.0–146.0	49.45	150	157.6	–10.6	0.077			
	5	1	42.0–44.0	50.43	150	111.7	43.5	0.098			
	5	2	12.0–14.0	51.63	150	67.0	25.0	0.129			
	6	2	36.0–38.0	61.37	150	87.0	46.8	0.079			
	6	3	52.0–54.0	63.03	150	157.1	–0.7	0.176			
	6	4	24.0–26.0	64.25	150	341.9	–21.4	0.039			
	7	1	59.0–61.0	69.60	150	214.8	52.7	0.141			
	7	2	52.0–54.0	71.03	150	314.4	–8.1	0.040			
	7	3	71.0–73.0	72.72	150	353.9	45.7	0.027			
	8	1	81.0–83.0	79.32	150	357.5	–33.4	0.034			
	8	2	16.0–18.0	80.17	150	355.9	–53.0	0.139			
	9	1	143.0–145.0	89.44	150	96.4	–31.3	0.097			
	10	1	65.0–67.0	98.16	150	137.1	–1.9	0.140			
	11	2	6.0–8.0	108.57	150	211.6	9.9	1.397			
	11	3	12.0–14.0	110.13	150	140.0	–4.2	0.121			
	11	3	144.0–146.0	111.45	150	277.6	–63.1	0.149			

The intensity on the outer rise and in the lower part of lower slope (Sites 487 and 488) is on the order of 10^{-5} emu/cc, which is one order stronger than in the middle and upper parts of lower slope (Sites 491 and 492), as follows:

Site	Average Intensity of Remanent Magnetization after 150-Oe AF Demag. (emu/cc)	No. of Samples	Rate of Sedimentation (m/m.y.)	Water Depth (m)
492	$10^{-6.2 \pm 0.8}$	8	14.8	1935
491	$10^{-6.2 \pm 0.8}$	5	31.9	2883
488	$10^{-5.0 \pm 0.7}$	17	374	4254
487	$10^{-5.2 \pm 0.4}$	21	19–420	3500–4764

These data indicate the existence of a boundary (which I will call "magnetization boundary") among the sediments with different intensities of remanent magnetization. On the continental side, the boundary is located between Sites 488 and 491 (2883–4254 m water depth). On the ocean side, because the sediments at Site 487, on the outer rise, have a stronger magnetization intensity and because the water depth is increasing from 3500 to 4764 meters with the Cocos Plate motion, the boundary is located above 3500 meters. The boundary is nearly horizontal at a water depth slightly shallower than that of the outer rise and this boundary line intersects the constant sedimentation rate line as shown in Figure 19.

Magnetization intensity in sediments is controlled by the amount and grain size of magnetic minerals. Because there is no significant difference in grain size distribution of sediments among the lower slope sites, the effect of grain size on intensity may be ignored. Thus magnetization intensity is controlled mainly by the magnetic mineral content. The intersection of the magnetization boundary line and constant rate lines suggests that the magnetic minerals are separated by turbidity currents. The magnetic minerals are concentrated in the lower sediments below the magnetization boundary, which, as I have noted, is nearly horizontal and slightly shallower than the water depth of outer rise. Unless the relation of depth between the boundary and outer rise has changed in the past, the intensity of magnetization may provide a paleobathymetric indicator.

There are also noticeable changes in the remanent magnetization intensity in a sedimentary sequence from the lower slope area at Sites 491 and 492 (Figs. 14 and 15); in the upper section of the sedimentary sequence the intensity is on the order of 10^{-6} emu/cc and in the lower section 10^{-5} emu/cc. The transition between the upper and lower sections is limited to a 10-meter area. Because the values of intensity in the lower section are similar to those in sediments accumulated during the last 0.69 m.y. at Sites 488 and 487, below the magnetization boundary water depth, I believe that the changes in intensity of remanent magnetization occurred when the site traveled across the magnetization boundary. This

belief is supported by the fact that no such changes in intensity occur in the sites located below the water depth of the magnetization boundary (Figs. 10 and 11).

The sediments from the lower slope area may be classified (from bottom to top) into three facies: thick layers of sand, mud with thin sand layers, and mud. Subdepth and age of the boundaries of these facies and the magnetic intensity transitions are as follows:

Site	Distance from Trench (km)	Subdepth (m) and Age (m.y.) of the Boundaries Mud/Mud with Sand	Mud with Sand/Sand	Magnetic Intensity Transition
492	22.8	129.5 (6.0)	247 (8.6)	228 (8.1)
491	16.7	76 (2.6)	256 (5.0)	75 (2.6)
488	6.6	105 (0.3)	410 (0.9)	— (—)

The three facies are considered to represent the relative distance or relative height from the turbidite axis, the coarser-grained facies corresponding to locations closer to the turbidite axis. The Middle America Trench, which presently contains turbiditic sands, as at Site 486, must have done so as far back as 9 Ma, because the same kind of sand with the same magnetic properties (Type T) from 8.6 Ma was recovered from the uppermost part of the lower slope at Site 492. The general facies change from sand to mud in the lower slope means that the height of the lower slope surface relative to the trench bottom has increased with time. Age of the boundaries between the facies increases with the distance of the site from the trench (Fig. 20). Although the age of the magnetic intensity transition also increases with the distance from the trench, the gradient of age against distance is steeper than that of the facies boundaries, and the magnetic intensity transition is located in different facies at different sites. At Site 492 the transition occurs in the lower part, which is mud with thin sand layers; at Site 491 it is just above the upper boundary, which is mud with thin sand layers; and Site 488 has not yet reached the transition in spite of accumulating mud (Fig. 20). This change in relation between facies and the intensity transition indicates that the trench is relatively shallower with increasing age. At Site 492, the magnetic intensity transition is at a horizon close to the thick sand layer. This indicates that the depth of the trench relative to the outer rise was not great when these thick sand layers accumulated.

ORIENTATION ANALYSIS OF BEDDING PLANE AND FAULT PLANE

Positions of strata and faults are fundamental to geologic structure, and determining them is important to a reconstruction of the tectonic evolution of the area. Dip of bedding plane has never been measured directly in the holes drilled by *Glomar Challenger*, because the diameter of the bore holes is too small for the ordinary dip meters used in oil wells. During Leg 66 we attempted to determine the orientation of bedding and fault planes by means of paleomagnetic direction.
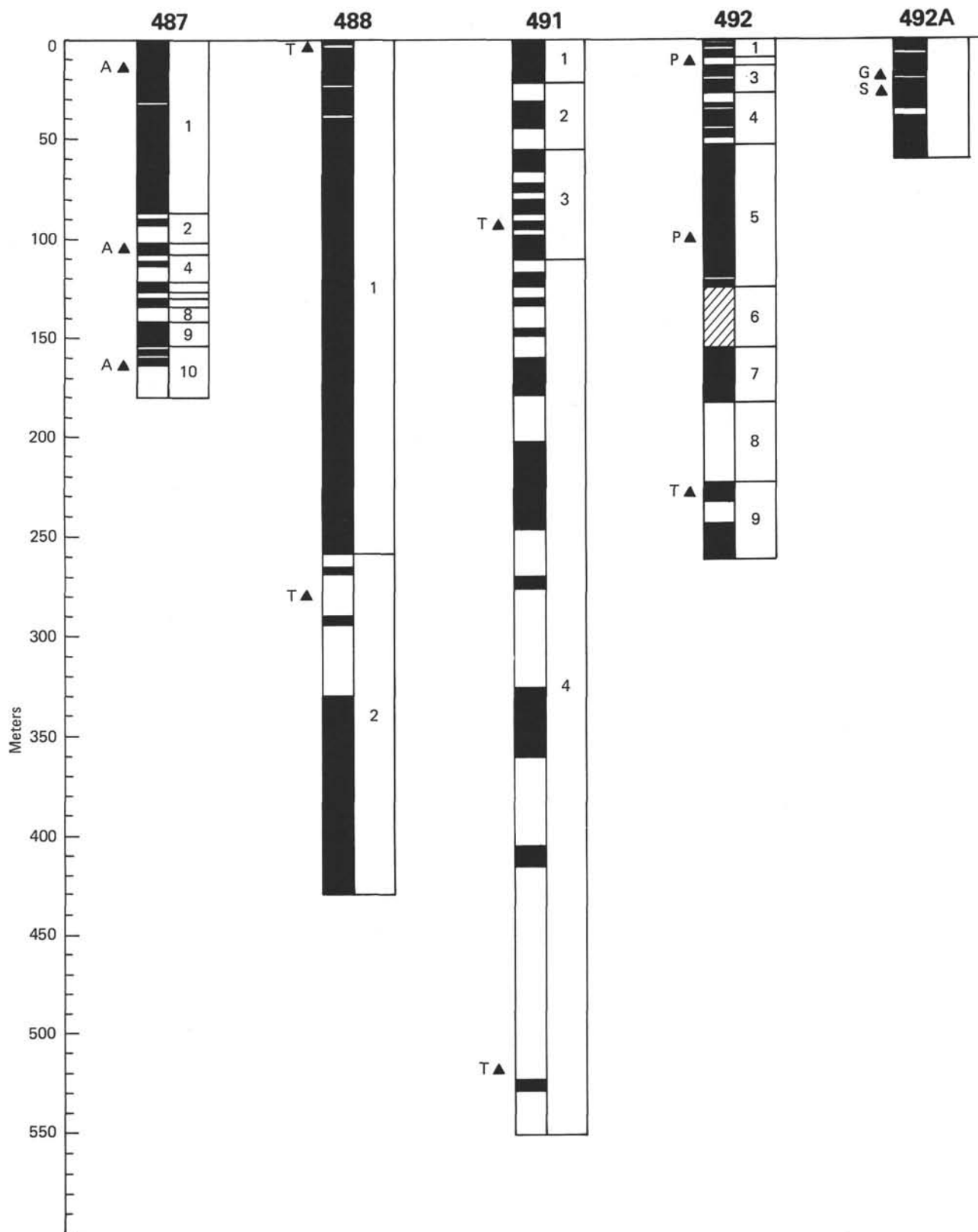
Figure 18. Magnetostratigraphic correlation of Leg 66 holes. (▲ = horizons of samples for stepwise AF demagnetization test [Fig. 2], black = normal polarity, white = reversed polarity.)
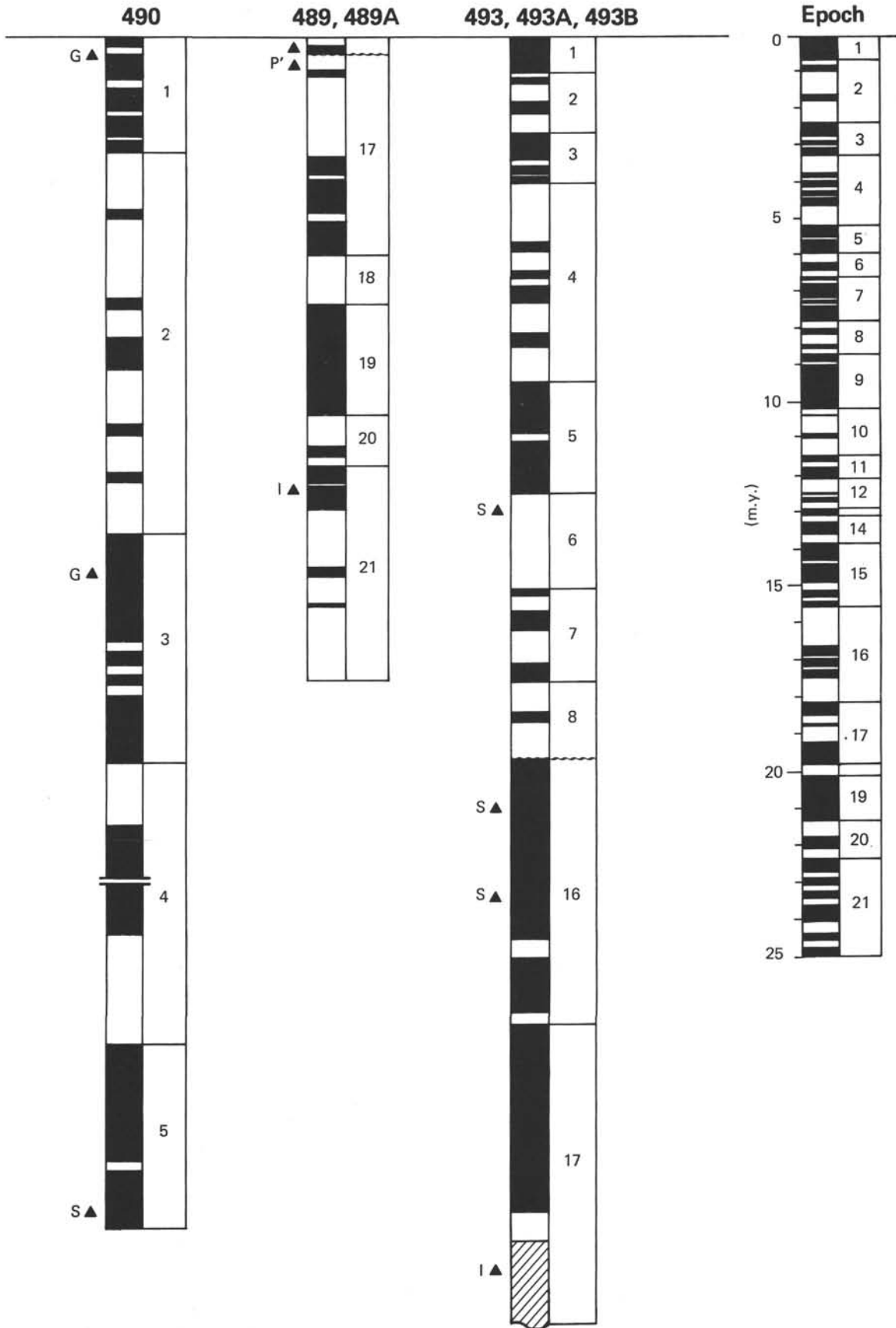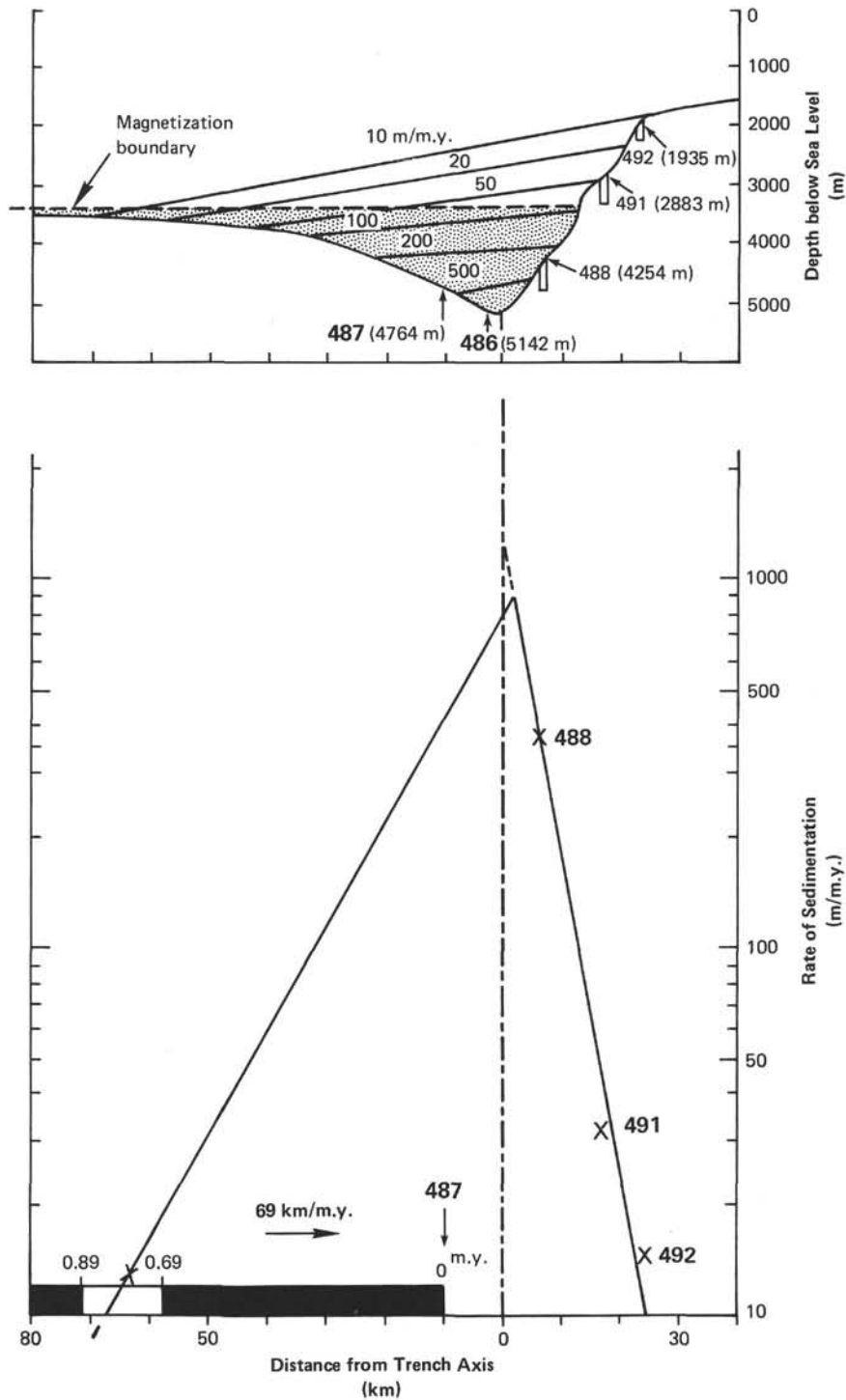
Figure 18. (Continued).

Figure 19. Rate of sedimentation during the last 0.69 m.y., Middle America Trench area. (Top graph): relation between rate of sedimentation and submarine topography; (bottom graph): relation between rate of sedimentation and distance from trench axis. (Broken line indicates magnetic boundary. In dotted area below the boundary, sediments have a magnetic intensity of approximately 10^{-5} emu/cc.)

The principle is essentially the same as using a magnetic compass in the field. The only difference being the focus on past instead of present geomagnetic field. We can measure the declination of remanent magnetization after correction for dip of bedding plane and dip direction of bedding against the core tube. Orientation is possible with the following assumptions: (1) The declination of geomagnetic field was 0° (due north) during normal polarity and 180° (due south) during reversed polarity; (2) geomagnetic polarity can be determined with the inclination of remanent magnetization; (3) drilling axis is vertical; and (4) axis of folds are not
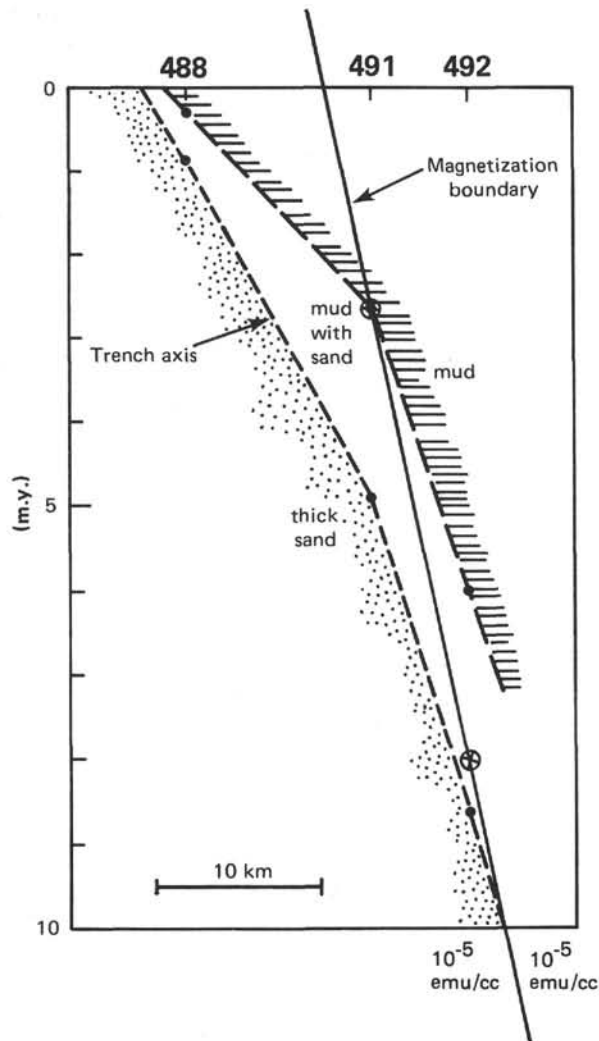
Figure 20. Ages of lithofacies boundaries and magnetization boundary, lower slope area.

Figure 21. Bedding directions in the lower slope. Pole of bedding plane is projected on lower hemisphere of the stereo net. A, Site 492; B, Site 491; C, Site 488. (For an explanation of A, B, C, D, and E see text, Fig. 23, and Table 11. • = bedding direction below 415 m sub-bottom at Site 491.)

plunging (i.e., horizontal). In the low latitude area, the deviation of declination of the present geomagnetic field is less than 20°. The polarity of the ancient geomagnetic field can be estimated by an inclination of remanent magnetization larger than 10°. The deviation of drilling axis measured during Leg 66 was within 3° of the vertical.

Bedding Orientation in the Lower Slope

Inclined beds occurred below 350 meters subdepth in the lower part of the Site 488 lower slope, below 100 meters subdepth in the middle part of the Site 491 lower slope, and below 110 meters subdepth in the upper part of the Site 492 lower slope. Orientation of bedding plane was determined at 60 horizons.

At Site 488, the dips determined at three horizons agree with each other (20°–35° east-northeast) (Fig. 21C and Table 8). The east dip in an upslope direction is consistent with seismic reflection data (Shipley et al., 1980).

In Site 491 sediments below 100 meters subdepth, the dips of 44 bedding planes are oriented; they dip from 4° to 64° in a generally north-northeast direction, which is

opposite to the direction of submarine topographic slope (Fig. 21B and Table 11). In five limited intervals the sediments dip southwestward, and the dip angle changes. The interval from 120 to 135 meters subdepth (A in Fig. 21B) is a transition between the upper hori-

zontal and the lower inclined beds. In the interval from 160 to 170 meters (B in Fig. 21B), the upper 30°–40° dipping beds grade into lower horizontal beds. The interval from 250 to 285 meters (C in Fig. 21B) has steep dips (60°) in the upper part and lower, gentle dips (15°–30°) in the lower part. Below a subdepth of 285 meters (D, in Fig. 21B) the southwestern dip attains a maximum of 45° at 345 meters and is 41° from 400 to 425 meters, where a brecciated zone with poor recovery occurs. The general strike of both bedding planes is N60°W, parallel to that of lower slope surface and trench axis (Fig. 22).

Sediment layers at Site 492 below 110 meters subdepth dip from 14° to 74° and are partly overturned. Dips were measured at 13 horizons. The layers strike N40°E, perpendicular to the submarine ridge to the north of this site (Fig. 22). The dip directions are northwest and southeast, as shown in Figure 21A and listed in Table 12. Southeasterly dips were limited to the interval from 160 to 231 meters subdepth (E in Fig. 21A). With regard to the dip direction, this interval from 160 to 230 meters forms the middle part of the sediments recovered at Site 492. The lower segment of the upper part, between 125 and 160 meters subdepth, was brecciated by

tectonic disturbance, and no paleomagnetic samples could be collected. The middle part has steeper dips than the others, and the steepest dip (74°) is observed at 214 meters subdepth.

In the lower slope area, the horizon with downslope dip are limited to intervals associated with dip angle variation and tectonic brecciation. This implies that upslope dip direction is the normal attitude of the bedding planes and that downslope direction is a result of tectonic deformation. The alternating occurrence of upslope and downslope dips can be explained as parts of an anticline in which axial planes are inclined upslope, possibly as a result of thrusting, as illustrated in Figure 23. Seismic reflection data revealed the same type of thrusting and related deformation beneath the lowest part of the lower slope (Shipley et al., 1980). This deformation is part of the accretionary process caused by subduction of the oceanic plate along the continental margin. Displacement on this thrust must be small, because the magnetobiostratigraphic succession is undisturbed; we found neither disordered biostratigraphic markers nor disordered magnetostratigraphic sequences in the lower slope area.
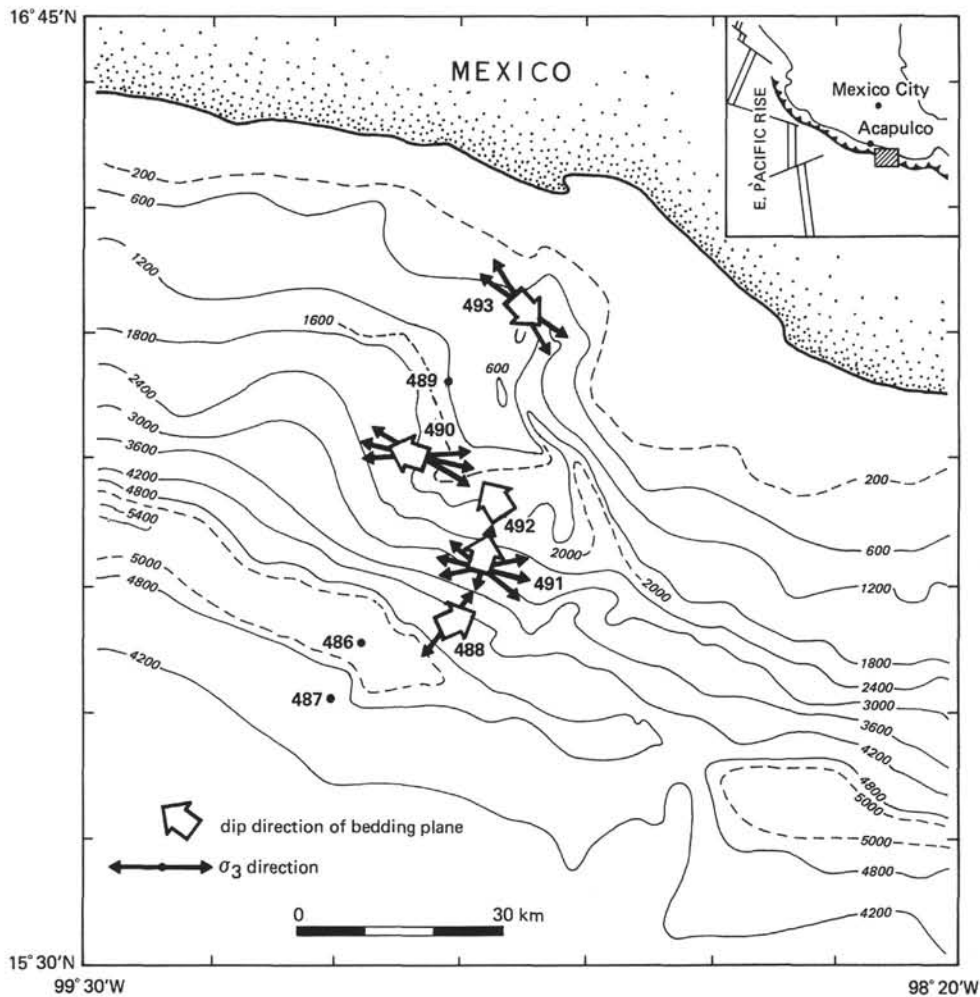

Figure 22. Dipping direction of bedding plane and direction of minimum compressional (or tensional) axis of stress field in Leg 66 area.
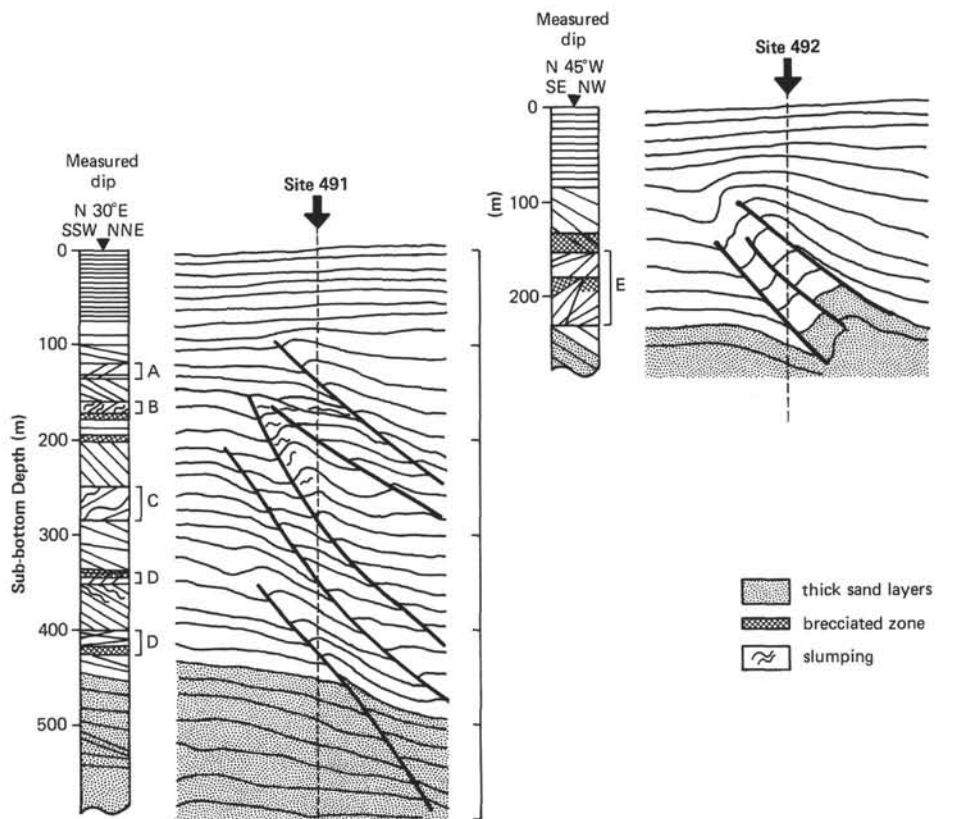
Figure 23. Variations with sub-bottom depth in dip and dip direction of bedding plane, slumping, and tectonic brecciation, Sites 491 and 492, lower slope.

Bedding Orientation in the Upper Slope

Forty inclined beds were oriented in the outer part of the upper slope at Site 490, where sediments below 345 meters subdepth ranged in dip from 10° to 81°. Dip directions of the bedding planes are shown in Figure 24B and Table 10. Most of the dips are westward; a few are northward. Mean and standard deviation of the dip directions are N80° ± 25°W. This direction corresponds to that of the topographic slope in the area of Site 490. Bedding dips below 350 meters gradually increase with depth. Between 400 and 430 meters subdepth, sediments dip 10° to 75° westward and are cut by slickensided normal faults and oblique slip faults with a brecciated zone. Below this fault zone, the bedding dips gradually decrease with increase of depth. This change indicates that the normal faults caused the steep bedding dips (Fig. 25).

We measured the dips of 37 inclined beds in the inner part of the upper slope at Site 493 (Table 13). The sedimentary sequence of this site comprises the upper part of the upper Miocene to the present, overlying the lower part of the lower Miocene with an unconformity at 360 meters subdepth. The upper part is almost horizontal except for the possibly slumped beds at 278 and 286 meters subdepth. The slumped beds strike N20°E parallel to submarine ridge to the east of this site (Figure 24A), suggesting that the uplift of the submarine ridge

and related slumping occurred in the late Miocene, Epoch 6. The dip angle of the lower part ranges from 0° to 39° in a generally southeast direction parallel to but steeper than the submarine topographic slope. A northwestward dip was observed in two limited intervals from 370 to 380 meters (A in Fig. 24A) and from 435 to 507 meters (B in Fig. 24A) subdepth.

Tectonic features revealed in the upper slope are mostly normal faults dipping in a downslope direction, accompanied by drag folds in contrast with thrusts dipping in an upslope direction in the lower slope. The difference in tectonic configuration indicates the difference in tectonic forces between the two areas.

Orientation of Fault Planes and Stress Fields

Fault planes can be oriented in the same manner as bedding planes. If we find a conjugate set of faults, an estimation of stress field is possible using the fault plane orientation and fault displacement. The fault planes and stress fields were oriented at six horizons at Sites 488 and 491 on the lower slope and at five horizons of Sites 490 and 493 on the upper slope.

Many artificial fractures had been produced by drilling and handling, as mentioned earlier and noted by Lundberg and Moore (this volume). Such artificial fractures were eliminated for this study by using the nature of the fracture surface and systematic orientation with sawn surface.
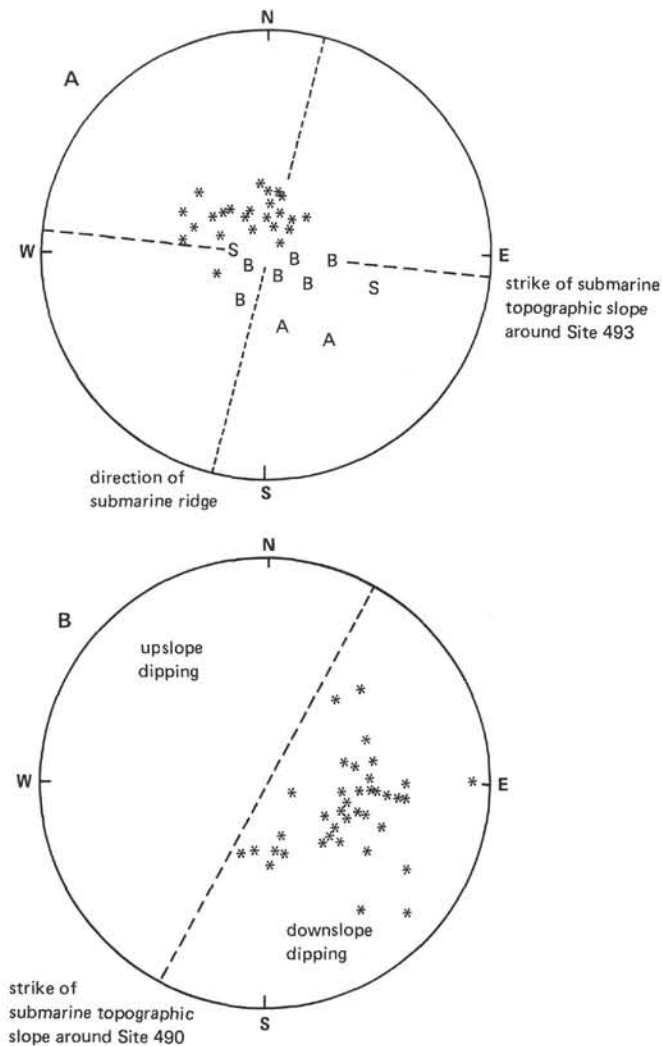
Figure 24. Bedding direction of upper slope. Pole of bedding plane is projected on lower hemisphere of stereo net. A, Site 493; B, Site 490. (For an explanation of A, B, and S see text and Table 13.)

Figure 25. Variations with sub-bottom depth in dip and dip direction of bedding plane, Site 490, upper slope.

Lower Slope

The stress field is determined at 383 meters subdepth at Site 488 and at five horizons in the interval from 516 to 524 meters subdepth at Site 491 (Table 14). At five of the six horizons, the stress fields have a nearly vertical axis of maximum compressional stress corresponding to the direction of gravity and overburden pressure. At 441.00 meters subdepth at Site 491, the stress field has a maximum compressional axis plunging at 38°, suggesting that the horizontal compressional stress was comparable to the vertical compressional stress.

The determined stress fields may be divided into two groups, using the horizontal stress condition: One has a minimum compressional (or tensional) axis subparallel to trench axis; the other has a minimum compressional axis perpendicular to the trench axis. The stress perpendicular to the trench axis is compressional or tensional in different places within a single hole. The two states may exist within a 1-meter interval—for example, at 523.13 meters and 523.89 meters subdepth at Site 491.
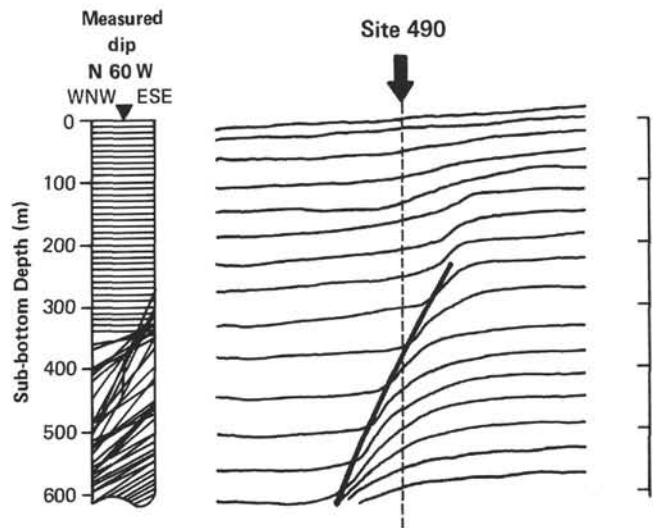
The difference is probably associated with drag folding and thrusting at shallow subdepth.

Upper Slope

Many faults with slickensided surfaces were observed in the lower part of the sediments at Site 490, ranging in subdepth from 400 to 430 meters. Three sets of conjugate faults were oriented and stress fields estimated (Table 15). The maximum compressional axis is almost vertical and the minimum compressional axis is horizontal in an east–west direction. The direction of the minimum compressional axis is concordant with the dip direction of bedding plane (Fig. 22). The steep dip of bedding plane in this interval could have been caused by a drag fold associated with a dipping normal fault, which was formed in the east–west minimum compressional stress field. The westward slope of submarine topography can be explained as a result of this tectonic movement (Fig. 25).

At Site 493, several conjugate fault sets and fracture zones were observed in the lower part of the cored section between 560 and 580 meters subdepth. Two stress fields were determined from the conjugate sets (Table 15). The minimum compressional axis is horizontal in a northwest–southeast direction, which agrees with the predominant dip directions of bedding planes (Fig. 22).

The stress field in the upper slope is uniform with the maximum compressional axis vertical, the intermediate axis perpendicular to the trench axis, and the minimum compressional axis parallel to the trench axis. This means that the horizontal compressional stress is smaller than the vertical compressional stress, corresponding to the overburden, and the normal faults trend perpendicular to the trench axis (parallel to the horizontal compressional axis) on the upper slope.

CONCLUSIONS

The paleomagnetic studies of sediments and basement rocks from the Middle America Trench off Mex-

Table 14. List of orientation of conjugate fault planes and stress field, lower slope.

Hole	Core/Section	Sub-bottom Depth (m)	Orientation of Conjugate Fault Planes	Stress Field		
				σ_1	σ_2	σ_3
491	49-3, 50 cm	441.00	N 50E 59E N 3W 48E	N63W38D	S88E48D	S17W12D
	57-3, 31 cm	516.81	N 71E 44N N 9E 56E	S46W60D	N33E30D	S53E5D
	57-3, 146 cm	517.96	{ N 61W 37E { N 7W 28E	S37E77D	N11W10D	S79W5D
	58-1, 13 cm	523.13	{ N 6E 40W { N 40E 52W { N 23E 76E { N 34E 47E	N6E75D	S22W13D	S69E3D
	58-1, 89 cm	523.89	EW 33N { N 15W 33W { N 47W 33W	S69E72D	N52W19D	S27W1D
488	42-2, 16 cm	382.66	N 54W 68N N 50W 61S	S53E74D	N48W15D	N42E3D

Note: σ_1 = maximum compressional axis, σ_2 = intermediate axis, σ_3 = minimum compressional or tensional axis, { = curved fault plane.

Table 15. List of orientation of conjugate fault planes and stress field, upper slope.

Site	Core/Section	Sub-bottom Depth (m)	Orientation of Conjugate Fault Planes	Stress Field		
				σ_1	σ_2	σ_3
493	48-1, 80 cm	557.80	N 67E 27N N 18E 58E	S77W64D	N30E18D	S54E17D
	48-1, 90 cm	557.90	N 48E 75N N 70E 66S	N64E61D	S45W28D	N32W5D
	44-2, 125 cm	401.25	N 5E 71W (N52W69D) N 10E 52E (N87E54D) N 5E 73W	S38E72D	N1E14D	S88W12D
490	47-1, 67 cm	423.17	(S34W57D) { N 8W 59E { (S49E46D) N 18W 36W (S44W32D)	S23E72D	N1E14D	S89W8D
	48-1, 83 cm	427.83	N 9E 40W (S41W23D) N 38E 60E (S5E52D)	N8W62D N4W71D	S22W25D S28W16D	S74E13D S65E10D

Note: σ_1 = maximum compressional axis, σ_2 = intermediate axis, σ_3 = minimum compressional or tensional axis { = curved fault plane, ( ) = direction of slickenside.

ico during Leg 66 reveal several charactric magnetic properties. The remanent magnetization of sediment samples can be divided into seven types on the basis of reaction to stepwise AF demagnetization. The normal–reverse tests and inclination analysis indicate that the most of the remanent magnetization are reliable for paleomagnetic investigations after 150-Oe AF demagnetization.

Basalts recovered from the outer rise at Site 487 have characteristics typical of ocean basalt containing maghemitizated titanomagnetite grains and possessing stable remanent magnetization; titanium content in the magnetite is remarkably low, however. Intensity of remanent magnetization in metamorphic and plutonic rocks recovered from the upper slope area at Sites 489 and 493 is too weak to produce the observed magnetic anomalies over the upper slope area.

Magnetostratigraphically the sedimentary sequences range in age from Recent to Early Miocene and have been classified into Epochs 1 through 21, which permits a quantitative estimate of sedimentation rate by correlation with an established geomagnetic time scale. The rate of sedimentation in the area along the Middle America Trench decreases with distance from the trench. The evolution of the sedimentation rate, sedimentary facies, and changes in magnetic mineral content indicate that the initiation of subduction and accretion under the lower slope area occurred about 10 Ma.

Orientations of bedding and fault planes are determined by paleomagnetic direction. On the lower slope, the bedding planes dip landward (upslope). On the upper slope, the bedding planes dip downslope. Calculated stress field from the conjugate fault directions are consistent with the direction of plate convergence, the minimum compressional axis or tensional axis parallel to the Middle America Trench.

REFERENCES

Akimoto, S., 1962. *J. Phys. Soc. Jpn.*, 17(B-1):706.
Ishihara, S., 1977. The magnetite-series and ilmenite-series granitic rocks. *Mining Geol.*, 27:293–305.
Johnson, H. P., 1979. Magnetization of the oceanic crust. *Rev. Geophys. Space Phys.*, 17:215–226.
Minster, J. B., and Jordan, T. H., 1978. Present-day plate motions. *J. Geophys. Res.*, 83:5331–5354.
Niitsuma, N., 1977. Remanent magnetization of slumped marine sedimentary rocks. *Rock Magn. Paleogeophys.*, 4:44–52.
Ryan, W. B. F., Cita, M. B., Rowson, M. D., et al., 1974. A paleomagnetic assignment to Neogene stage boundaries and the development of isochronous datum planes between the Mediterranean, the Pacific and Indian oceans in order to investigate the response of the world ocean of the Mediterranean "salinity crisis." *Riv. Ital. Pal.*, 80:631–638.
Shipley, T. H., McMillen, K. J., Watkins, J. S., et al., 1980. Continental margin of Guerrero and Oaxaca, Mexico. *Mar. Geol.*, 35:65–82.
Yaskawa, K., Nakajima, T., Kawai, N., et al., 1973. Palaeomagnetism of a core from Lake Biwa (1). *J. Geomagn. Geolelectr.*, 25:447–474.
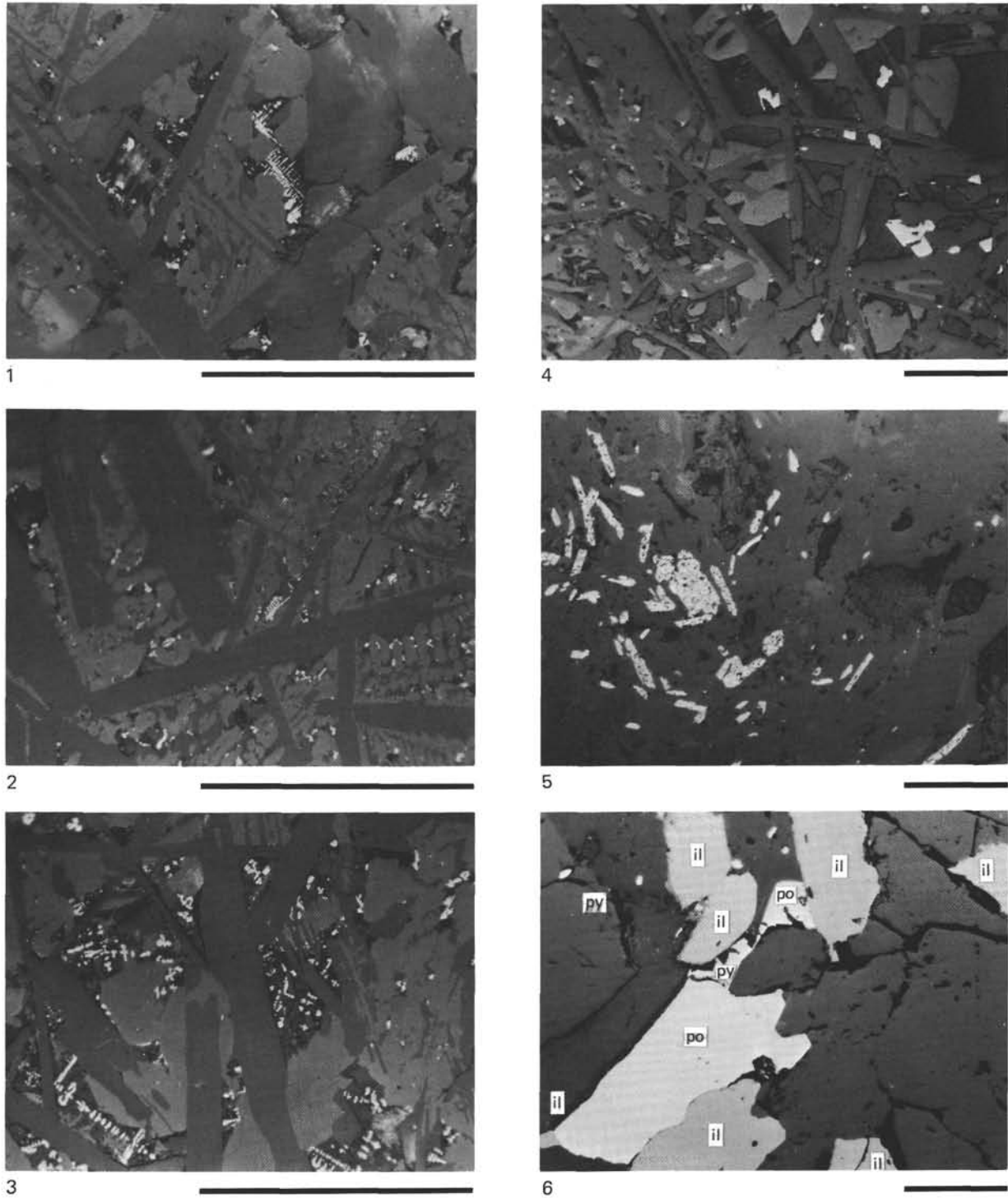
Plate 1. Reflective micrographs of basement rocks in the outer rise and upper slope of the Middle America Trench area off Mexico (scale bar = 100 μm). 1. Skeletal maghemitizated magnetite in abyssal basalt, Section 487-20-1 (Piece 2, 172.10 m sub-bottom). 2. Skeletal maghemitizated magnetite in ocean basalt, Section 487-20-1 (Piece 13, 172.94 m sub-bottom). 3. Skeletal maghemitizated magnetite in ocean basalt, Section 487-20-1 (Piece 17, 173.19 m in sub-bottom). 4. Cubic and skeletal maghemitizated magnetite in ocean basalt, Section 487-20-1 (Piece 17, 173.19 m in sub-bottom). 5. Lath-shaped rutile in metamorphic rock, Section 489A-34-1 (Piece 6, 318.06 m in sub-bottom). 6. Ilmenite (il), pyrrhotite (po), and pyrite (py) with granular shape in plutonic rock, Section 493-59-2 (Piece 9, 658.75 m sub-bottom).